ACS APPLIED NANO MATERIALS

Article

Hollow Zinc Oxide Microsphere-Multiwalled Carbon Nanotubes Composites for Selective Detection of Sulfur Dioxide

Ni Luh Wulan Septiani, Adhitya Gandaryus Saputro, Yusuf Valentino Kaneti, Arifin Luthfi Maulana, Fadjar Fathurrahman, Hyunsoo Lim, Brian Yuliarto, * Nugraha, Hermawan Kresno Dipojono, Dmitri Golberg, and Yusuke Yamauchi

ACS Appl. Nano Mater., **Just Accepted Manuscript** • DOI: 10.1021/acsanm.0c01707 • Publication Date (Web): 31 Aug 2020

Just Accepted

is published by the American Chemical Society. 1155 Sixteenth Street N.W., Washington, DC 20036

Hollow Zinc Oxide Microsphere-Multiwalled Carbon Nanotubes Composites for Selective Detection of Sulfur Dioxide

Ni Luh Wulan Septiani,[1] Adhitya Gandaryus Saputro,[1] Yusuf Valentino Kaneti[2,*] Arifin Luthfi Maulana,[1] Fadjar Fathurrahman,[1,3] Hyunsoo Lim,[4] Brian Yuliarto,[1,3,*] Nugraha,[1,3] Hermawan Kresno Dipojono,[1,3] Dmitri Golberg,[2, 5*] Yusuke Yamauchi[2,4,6*]

[1] *Engineering Physics Department, Institute of Technology Bandung, Bandung 40132, Indonesia*

[2] *World Premier International (WPI) Research Center for Materials Nanoarchitectonics (MANA), National Institute for Materials Science (NIMS), 1-1 Namiki, Tsukuba, Ibaraki 305-0044, Japan*

[3] *Research Center for Nanosciences and Nanotechnology (RCNN), Institute of Technology Bandung, Bandung 40132, Indonesia*

[4] *School of Chemical Engineering & Australian Institute for Bioengineering and Nanotechnology (AIBN), The University of Queensland, Brisbane, QLD 4072, Australia*

[5] *Centre for Materials Science and School of Chemistry and Physics Queensland University of Technology (QUT), Brisbane, QLD 4000, Australia*

[6] *Department of Plant and Environmental New Resources, Kyung Hee University, 1732 Deogyeong-daero, Giheung-gu, Yongin-si, Gyeonggi-do, 446-701, South Korea*

E-mails: KANETI.Valentino@nims.go.jp; brian@tf.itb.ac.id; dmitry.golberg@qut.edu.au; y.yamauchi@uq.edu.au

Abstract

This work reports the first utilization of anthocyanin extracted from black rice (*Oryza sativa L.*) grains as a structure-directing agent for the synthesis of hollow zinc oxide (ZnO) spheres *via* a simple solvothermal reaction and their subsequent modifications with various amounts of multiwalled carbon nanotubes (MWCNTs). Following hybridization with MWCNTs, some MWCNTs are observed to penetrate into the inner cavities of the spheres, while ZnO nanoparticles are formed on the surface of some MWCNTs. When employed as a sulfur dioxide (SO_2) sensor, the ZnO-MWCNT (15:1) composite displays a high response of 156 to 70 ppm of SO_2 at an optimum temperature of 300 °C as well as good selectivity to SO_2 with the response to 50 ppm of SO_2 gas being three-times higher than those to other gases, such as CO, CO_2, methanol, toluene, hexane, and xylene. Interestingly, the sensing behavior of this composite is strongly influenced by the proportion of MWCNTs. Specifically, *n*-type sensing behavior is observed for both ZnO-MWCNT (10:1) and (15:1) composites, while *p*-type behavior is observed for the ZnO-MWCNT (5:1) composite. The switch in sensing behavior suggests the major contribution of *p*-type MWCNTs to the electronic and sensing properties of the ZnO/MWCNT composites. The density functional theory (DFT) simulations on the adsorption of SO_2 on ZnO/CNT system reveals that SO_2 molecule only chemically interacts with the O adatom of ZnO (*i.e.*, oxygen atom adsorbed on the surface of ZnO) to form sulfur trioxide (SO_3) and charge transfer is observed from ZnO to CNT, which creates a potential barrier at the ZnO/CNT interface and enhances the change in resistance of the composite sensor upon exposure to SO_2 gas.

Keywords: Zinc oxide, Porous metal oxides, Sulfur dioxide sensor, Gas-sensing, Carbon nanotubes, Nanocomposites

1. Introduction

Sulfur dioxide (SO_2) is considered as a toxic air pollutant in the atmosphere.[1-2] In general, SO_2 is generated by the combustion of sulfur-containing fuels in industries, automotive engines, and power plants.[3-4] Moreover, SO_2 is also released during natural events, such as volcanic eruptions and forest fires.[3, 5] The discharge of SO_2 gas into the atmosphere can have detrimental effects to both the environment and human health. Health problems, including eye/skin irritation, lung failure, cardiovascular disease, breathing difficulty, and even death can occur as a result of exposure to SO_2 gas.[5-6] In addition, the combination between SO_2 and NO_2 in the atmosphere can lead to acid rain that possesses danger to plants, aquatic animals, and infrastructure.[5, 7] To date, several different sensors have been developed for monitoring the concentration of SO_2 in air, including chromatography[8-9], surface accoustic wave (SAW)[10], laser-induced fluorescence[11], and chemiresistive gas sensors.[12] Among them, the chemiresistive gas sensor is widely popular due to its simple design, low manufacturing cost, ease of fabrication, high sensitivity, and good long-term stability.[7]

Various semiconducting metal oxides, such as zinc oxide (ZnO), tin oxide (SnO_2), tungsten oxide (WO_3), nickel oxide (NiO), titanium dioxide (TiO_2), and cobalt oxide (Co_3O_4), have been employed as sensitive gas-sensing materials for the detection of various hazardous gases.[13-20] The low cost, wide abundance, high sensitivity, good thermal and chemical stabilities, and non-toxicity of ZnO have made it highly attractive for gas-sensing applications.[21-23] Furthermore, as a *n*-type semiconductor with a wide band gap of 3.37 eV and large exciton binding energy of 60 meV, the resistance of ZnO is strongly dependent on the chemisorbed oxygen ions on its surface.[24-27] To date, various ZnO nanoarchitectures ranging from 0D (*e.g.*, nanoparticles, nanoclusters), 1D (*e.g.*, nanowires, nanoneedles, nanorods), 2D (*e.g.*, nanosheets, nanoplates, nanoflakes), and 3D (*e.g.*, nest-like and wool ball-like structures) nanostructures have been reported.[1, 28-35] Apart from shape control, ZnO-based nanostructures with various pore sizes, such as microporous, mesoporous, and macroporous ZnO have also been synthesized to enhance the specific surface area.[36] Among these, hierarchical ZnO nanostructures with mesoporous features have the advantages of high surface area and large pore volume due to their low density structure, which can promote high molecular transport to enhance the gas-surface interactions.[37-39]

The formation of hierarchical ZnO nanoarchitectures typically requires structure-directing agents that help the nanoparticles to assemble and build a specific structure. For instance, diethylene glycol (DEG) was employed in the synthesis of nanoparticle-assembled ZnO spheres.[40-41] In other reports, hexamethyltetraamine (HMTA) was used to produce ZnO hollow spheres which are assembled of nanosheets[42], while glycerol promoted the self-assembly of nanoflakes into wool ball-like ZnO structures.[43] In order to reduce chemical pollutants in the air and water, green synthetic approaches have been developed to subtitute synthetic chemical agents with naturally-derived chemicals. This approach is considered eco-friendly, low cost, and biocompatible.[44-45] Currently, there have been many reports on the utilization of chemicals extracted from plant extracts (*e.g.*, aspalathus linearis and pongamia pinnata extracts[46-47]), fruit rinds (*e.g.*, aloe vera and rambutan extracts[48-49]), and micro-organisms (*e.g.*, bacteria[44]) as structure-directing agents for controling the growth process of ZnO. However, the morphology of the resulting ZnO products has been limited to nanoparticles. Recently, some success have been achieved in synthesizing ZnO nanostructures with controlled 1D (*e.g.*, nanoneedles) and 2D structures (*e.g.*, nanoflakes) using naturally occurring compounds.[50] The resulting ZnO products however exhibit solid structures and/or aggregated, features which are not desirable for sensing applications. At present, it remains challenging to synthesize hollow ZnO nanoarchitectures with controlled morphology using biologically active compounds found in plants (phytochemicals). Hollow nanoarchitectures can offer higher surface areas (increased adsorption sites for gas molecules), enhanced gas diffusion, and greater structural stability due to fewer agglomerations. In most cases, ZnO-based sensors require high operating temperatures owing to the need for activation prior to interacting with gas molecules, hence leading to high power consumption and poor long-term stability.[1] Moreover, due to their high sensitivity, ZnO-based sensors typically suffer from low selectivity as they are unable to distinguish the target gas in the presence of other gases.[51-53] Therefore, modifications of ZnO with other sensing materials are necessary to address these critical problems.

In this work, we demonstrate for the first time, the utilization of anthocyanin extracted from black rice (*Oryza sativa L.*) grains as a structure-directing agent to construct nanoparticle-assembled hollow ZnO spheres with many cavities *via* a combination of solvothermal reaction and post-synthetic calcination in air at 350 °C for 2 h. The effects of important reaction parameters, such as the amount of anthocyanin and reaction

time were investigated to reveal the underlying formation mechanism. The as-prepared hollow ZnO spheres were subsequently modified with multiwalled carbon nanotubes (MWCNTs) at different atomic ratios from 5:1 to 15:1. The influence of MWCNT addition on the sensing performance of the ZnO hollow spheres, including response, selectivity, and optimum operating temperature was analyzed. Finally, the possible sensing mechanisms for pristine ZnO and ZnO-MWCNT composite sensors are proposed.

2. Experimental Section

2.1 Anthocyanin extraction from black rice grains

Black rice (*Oryza sativa L.*) was purchased from a traditional market in Bandung city, Indonesia. Prior to extraction, the black rice grains were washed with water for several times to remove dirt and subsequently dried at room temperature overnight. Black rice powder was obtained by grinding these grains (see **Figure S1**) using mortar and pestle. The anthocyanin extraction procedure was as follows: 100 g of black rice powder was dissolved in 200 mL of methanol solution and stirred for 24 h in a dark room. After dissolution, the supernatant containing anthocyanin was separated using a centrifuge machine with a speed of 14000 rpm. To obtain the gel-like anthocyanin, the methanol in the solution was evaporated in a drying oven at 60 °C overnight and stored in a refrigerator for further processing.

2.2 Functionalization of multiwalled carbon nanotubes (MWCNTs)

The surface functionalization of MWCNTs was carried out according to previous reports.[1, 54] In a typical process, 300 mg of MWCNT powder was dispersed in a mixture solution (40 mL) containing nitric acid (HNO_3) and sulfuric acid (H_2SO_4) with a volume ratio of 3:1. The acid-modified MWCNTs were then stirred at 80 °C for 3 h following a short sonication. The functionalized MWCNT powder was collected by centrifugation and washed with distilled water several times until its pH became neutral, followed by drying at 80 °C overnight.

2.3 Anthocyanin-assisted synthesis of ZnO hollow spheres

ZnO hollow spheres were prepared *via* an anthocyanin-assisted solvothermal method. Typically, 0.5 mmol of $Zn(NO_3)_2{\cdot}6H_2O$ was dissolved in 40 mL of 2-propanol. Subsequently, a certain amount of the anthocyanin extract was added to the solution and sonicated for 1 h to obtain a homogeneous solution. The purplish solution was then transferred into a 100 mL stainless steel-lined Teflon autoclave and heated at 180 °C for 16 h. After cooling, the precipitate was collected by centrifugation and washed several times with ethanol to remove the unreacted substances. The as-prepared ZnO powder was obtained after drying at 80 °C overnight before being calcined in air at 350 °C for 2 h under a slow heating rate of 1 °C min^{-1}. To investigate the effect of anthocyanin on the morphology of ZnO, the amounts of anthocyanin extract were varied to 0.0103 g, 0.0206 g, and 0.0352

g. Furthermore, to understand the growth mechanism, the solvothermal reaction was carried out for different reaction times, including 2 h, 4 h, 8 h, and 16 h.

2.4 Synthesis of ZnO hollow spheres-MWCNT composites

To synthesize the ZnO-MWCNT composite, a certain amount of the MWCNTs was first dispersed in 40 mL of 2-propanol followed by sonication for 30 min. Then, 0.5 mmol of $Zn(NO_3)_2 \cdot 6H_2O$ was added into the suspension and stirred for 30 min. After that, 0.0103 g of the gel-like anthocyanin was added into the mixture solution and sonicated for 1 h until fully dissolved. Next, the mixture solution was placed into a 100 mL stainless-steel Teflon autoclave and reacted at 180 °C for 16 h. The product was collected by centrifugation, followed by washing several times with ethanol and subsequent drying at 80 °C overnight. ZnO-MWCNT powder was obtained after calcination at 350 °C for 2 h with a heating rate of 1 °C/min. ZnO/MWCNT composites with different ZnO:MWCNT ratios (15:1, 10:1, and 5:1) were prepared to determine the effect of the amount of MWCNTs on the gas-sensing properties of the composites.

2.5 Characterization

The crystallinity and phase composition of all products were characterized by X-ray diffraction (Rigaku Rint 2500X) with a Cu Kα source of radiation (λ = 1.5418 Å). The average crystallite size of each sample was calculated using the Scherrer's equation:

$$D = \frac{K\lambda}{\beta \cos\theta} \quad (1)$$

where D is the crystallite size, λ is the X-ray wavelength, K is Scherrer's constant (0.9), β is full-width at half-maximum (fwhm) value, and θ is the Bragg angle.The surface and interior morphology were checked using field-emission scanning electron microscope (FESEM) (Hitachi SU-8000) and transmission electron microscope (TEM) (Hitachi H9500). The IR spectra of anthocyanin and all prepared samples were collected using a Thermoscientific Nicolet 4700 spectrophotometer. Thermal decomposition behaviors of the samples were analyzed by thermogravimetric analysis (TGA) using a Hitachi HT-Seiko Instrument Exter 6300 TG/DTA in air with a heating rate of 10 °C min^{-1} from room temperature to 800 °C. Optical characterizations of all samples were performed using UV-visible spectroscopy (Thermoscientific Evolution 220) and the band gap of each sample was estimated from the Tauc's plot based on the equation:

$$\alpha hv = C(hv - E_g)^n \quad (2)$$

where α is the absorption coefficient, hv is the photon energy, C is proportionality constant, and E_g is the optical band gap. In this case, direct transition approach was used and the n value is ½. Nitrogen (N_2) adsorption-desorption measurements were conducted with a Belsorp-mini II Sorption System at 77 K. The specific surface areas of the samples were estimated using the Brunauer-Emmett-Teller (BET) method in the relative pressure (P/P_0) range of 0.05 to 0.30. All samples were degassed under vacuum at 150 °C for 16 h.

2.6 Sensor fabrication and gas-sensing measurements

Alumina substrates with silver (Ag) electrodes were used for the gas-sensing measurements. A thin film sensor was prepared by using the doctor blade technique. Typically, a certain amount of the sensing material was dispersed in ethylene glycol to form a slurry. This slurry was subsequently deposited onto the alumina substrate and dried at 200 °C for 1 h. The prepared film was placed in 1 L testing chamber and each electrode was connected to an external circuit through a gold needle. The change in the resistance of the sensor was recorded using a digital multimeter (Picotest M3500A). During the measurement, the sample was heated using an Omron G3PX-220EH instrument. The SO_2 concentration in the test chamber was monitored using the Bacharach PCA3 portable gas analyzer. Moreover, an air compressor was used to supply clean air into the testing chamber. In this study, the sensor response (S) was defined as $S = R_a/R_g$ (for n-type sensor) or $S = R_g/R_a$ (for p-type sensor), where R_a and R_g are resistances of the sensor under air and SO_2 atmospheres, respectively. The main gas-sensing measurements were carried out at a humidity level of 65%. To check the effect of humidity, we have also varied the humidity level to 80%. The cross-selectivity test was carried out by exposing the optimum ZnO-MWCNT composite to a mixture of 50 ppm of SO_2 and 50 ppm of the interfering gas. Prior to the exposure, fresh air was flown into the testing chamber to get a baseline. After a stable baseline was achieved, the gas mixture was introduced into the chamber and after 15 minutes of exposure, fresh air was flown into the chamber to purge it.

2.7 Density functional theory (DFT) calculations

Density functional theory (DFT) simulations have been proven to be useful tools for understanding the adsorption mechanisms of various gases on both inorganic and organic surfaces.[55-58] In this work, DFT simulations were employed to study the atomic interactions between CNT-ZnO system and SO_2 molecule. A

Zn_6O_6 cluster was used to model the ZnO nanoparticle. This cluster size is selected as it is small enough to accommodate the co-adsorption of SO_2 molecule and O adatom. The presence of O adatom is required to model the sensing mechanism of a chemiresistive gas sensor.[13, 59-62] The CNT is modeled using an armchair (8,8) CNT with diameter of 10.860 Å and length of 14.677 Å. This particular size of CNT is selected because it is large enough to accommodate the Zn_6O_6 nanocluster. Based on our initial DFT calculations, CNT without any defect could not bind well to the ZnO cluster. This is indicated by the low adsorption energy of -0.034 eV. A similar trend has been observed for Zn_2O_2 cluster adsorption on CNT or graphene.[63-64] Previous studies reported that metal cluster could be effectively adsorbed on a graphitic structure when the surface had a monovacancy (MV) defect and experimentally, functionalization of CNTs is typically required before it could bind with other materials, such as metals or metal oxides.[54, 65] We adopted this model to our CNT model by removing a C atom from the surface of CNT, *i.e.*, creating a surface carbon monovacancy ($CNT^{[MV]}$). By creating such vacancy, the Zn_6O_6 cluster could be adsorbed on the CNT surface ($CNT^{[MV]}/Zn_6O_6$) with a high adsorption energy of -2.40 eV, indicating a stable and strong adsorption. Since the adsorption of Zn_6O_6 cluster required the presence of carbon monovacancy, this caused the electronic structure of CNT to be semiconducting. Therefore, we expect that semiconductor CNT and metallic CNT will have similar Zn_6O_6 adsorption properties. The $CNT^{[MV]}/Zn_6O_6$ structure was used as a model foundation for studying the interaction with a single SO_2 molecule. The unit cell model of the $CNT^{[MV]}/Zn_6O_6$ configuration is shown in **Figure 1**.

The DFT calculations were performed using the Quantum-Espresso 6 package.[66] The generalized gradient approximation (GGA) was used to include the exchange-correlation effect, using the Perdew-Burke-Ernzerhof (PBE) functional.[67] The convergence of the electronic energy was achieved by using 30 Ry for the cutoff energy for plane-wave basis sets. We utilized the projector augmented wave formalism (PAW) to represent the valence-core interactions.[68] All electronic structure calculation was done at Gamma point. The effect of van der Waals interaction is described using the semi-empirical correction scheme of Grimme (DFT-D3). The calculation for isolated Zn_6O_6 cluster and SO_2 molecule was performed in a 30Å × 30Å × 30Å cubic cell. The systems were relaxed until the residual force on each atomic component was less than 0.025 eV/Å.

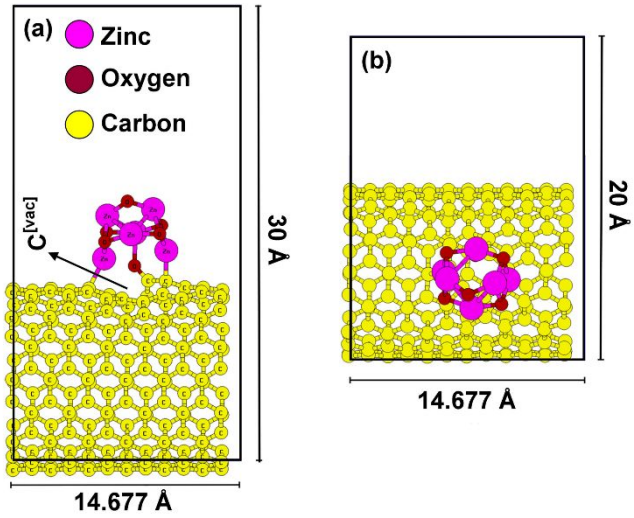

Figure 1. Side view (a) and top-view (b) of the optimized structure of the $CNT^{[MV]}/Zn_6O_6$ unit cell. The location of the carbon vacancy is indicated by $C^{[vac]}$.

All atoms were relaxed during the geometrical optimization. The adsorption energy of a molecule (E_{ads}) is defined as:

$$E_{\text{ads}} = E_{\text{system}} - E_{\text{surf}} + E_{\text{molecule}} \quad (3)$$

where E_{system} corresponds to the total energy of an adsorption system, E_{surf} corresponds to the total energy of a reference surface configuration and E_{molecule} corresponds to the total energy of an isolated molecule. Atomic charge calculations were performed using the Bader analysis.[69] The extra charges residing in an adsorbed molecule ($\Delta Q_{ads}^{SO_2}$) were defined as the difference between the total charges of an adsorbed SO_2 molecule with the total charges of an isolated SO_2 molecule. Visualizations of atomic structures and charge density were conducted using the XCrySDen software.[70]

3. Results and discussion

3.1. Morphology, composition, and formation mechanism

The major phytochemical present in the anthocyanin extracted from the black rice is identified to be cyanidine-3-O-glucoside based on our previous work[71] and other related studies.[72-75] FTIR spectroscopy was also carried out to confirm the presence of this compound, as seen in **Figure 2a**. The broad peak at around 3200-3400 cm^{-1} is attributed to the stretching vibration of O-H group, while the peaks at 2920 cm^{-1} and 2850 cm^{-1} correspond to the stretching vibration of C-H in aromatic and aldehyde group, respectively, in the glucose component of anthocyanin. Furthermore, stretching vibrations of C=O and C=C are marked by the peaks at 1710 cm^{-1} and 1600 cm^{-1}, respectively. The peaks between 1170-1500 cm^{-1} are assigned to the bending vibration of C-H and the peak at 1042 cm^{-1} is assigned to the stretching vibration of C-O.

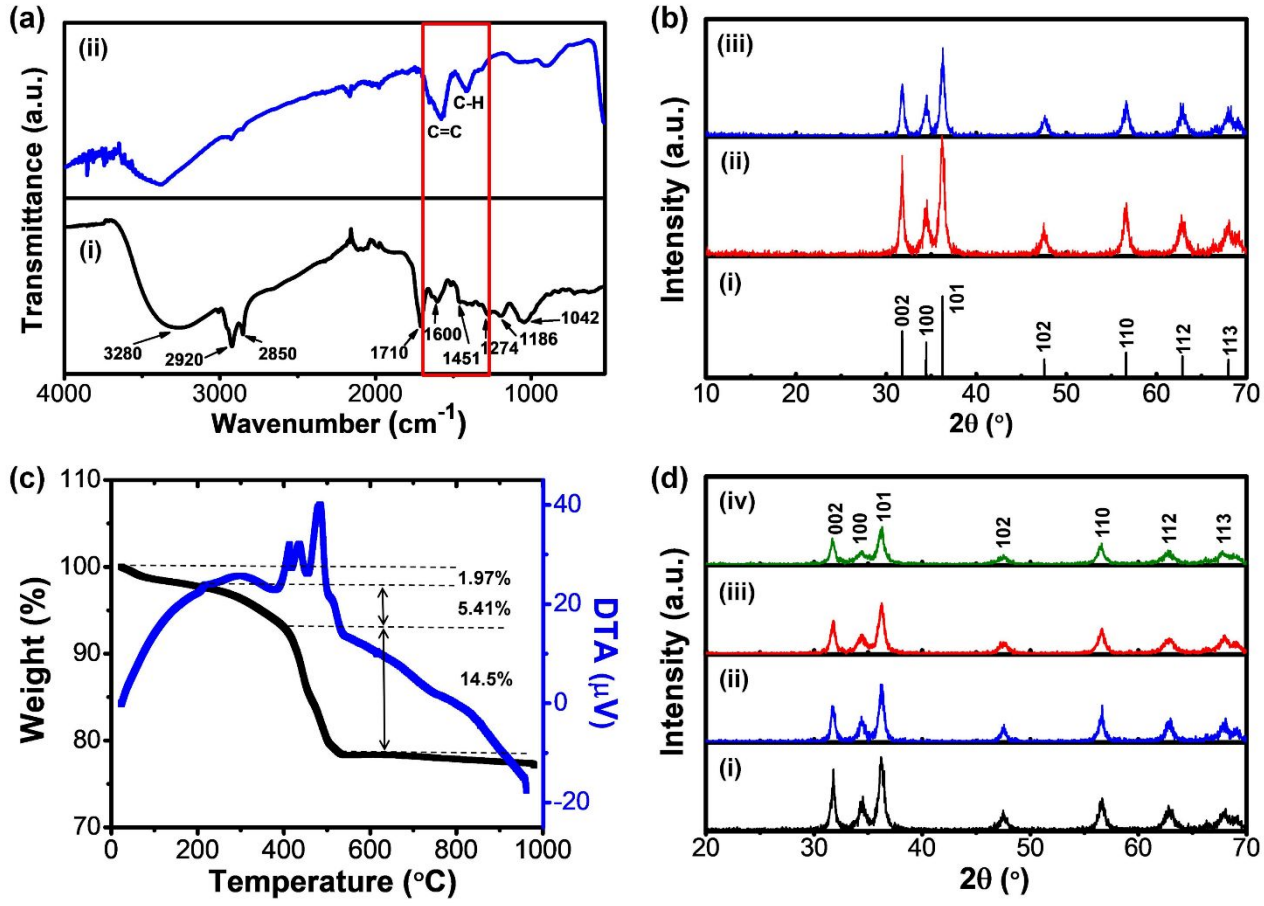

Figure 2. (a) FTIR spectra of anthocyanin extracted from black rice grains (i) and as-prepared ZnO (ii). (b) XRD patterns of standard hexagonal wurtzite ZnO (JCPDS No. 36-1451) (i), ZnO product obtained using the anthocyanin-assisted solvothermal reaction before (ii) and after calcination in air at 350 °C for 2 h (iii). (c) TG-DTA curve of the as-prepared ZnO sample in air from room temperature to 1000 °C. (d) XRD patterns of

ZnO-MWCNT composites obtained with ZnO/MWCNT atomic ratios of 1:0 (i), 15:1 (ii), 10:1 (iii), and 5:1 (iv).

The formation of the ZnO phase is readily observed following the solvothermal reaction at 180 °C, as shown in **Figure 2b**. This is supported by the presence of (100), (002), (101), (102), (110), (103), and (112) peaks of hexagonal wurtzite ZnO (JCPDS No. 36-1451).[76] However, the IR spectrum in **Figure 2a(ii)** and the TGA curve of the solvothermally-produced ZnO product reveal that it does not only contain ZnO crystals but also zinc complexes and anthocyanin residues or by-products. This is supported by the IR peaks at ~3400 cm^{-1}, ~1600 cm^{-1}, and 1451 cm^{-1}, which can be attributed to the stretching vibrations of O-H and C=C, and the bending vibration of C-H, respectively. The TG curve of the ZnO product obtained from the solvothermal process (**Figure 2c**) shows three weight loss steps. The initial weight loss of 1.97% occurring in the temperature range of 30-150 °C is due to the removal of physisorbed or chemisorbed water molecules. The second weight loss of 5.41% between 150-400 °C is attributed to the primary decomposition of the by-products of anthocyanin. Moreover, the highest weight loss of 14.5% is observed between 400-540 °C, which is due to the secondary decomposition of anthocyanin by-products (such as glucose) and recrystallization of ZnO. Moreover, the DTA curve shows three exothermic peaks corresponding to the crystallization of ZnO and the decompositon of anthocyanin. Following the calcination process at 350 °C, hexagonal wurtzite ZnO with lattice constants of a = 3.25 Å and c = 5.20 Å are obtained. The pristine MWCNTs display a strong peak at 26°, corresponding to the peak of carbon (graphite). The crystal structure of the MWCNTs is maintained after the acid treatment, indicating that no significant structural destruction has occurred during this process (**Figure S2**). In the case of the composites, no peak is observed at 2θ = 26°, suggesting that the addition of MWCNTs to the ZnO does not affect the formation of ZnO (**Figure 2d**). However, the intensities of the ZnO peaks are noticeably reduced with increasing content of MWCNTs. Based on the Scherrer's equation (Eq. 1), the average crystallite sizes of pure ZnO and ZnO-MWCNT (15:1), ZnO-MWCNT (10:1), and ZnO-MWCNT (5:1) composites are calculated to be 19 nm, 22 nm, 21 nm, and 19 nm, respectively.

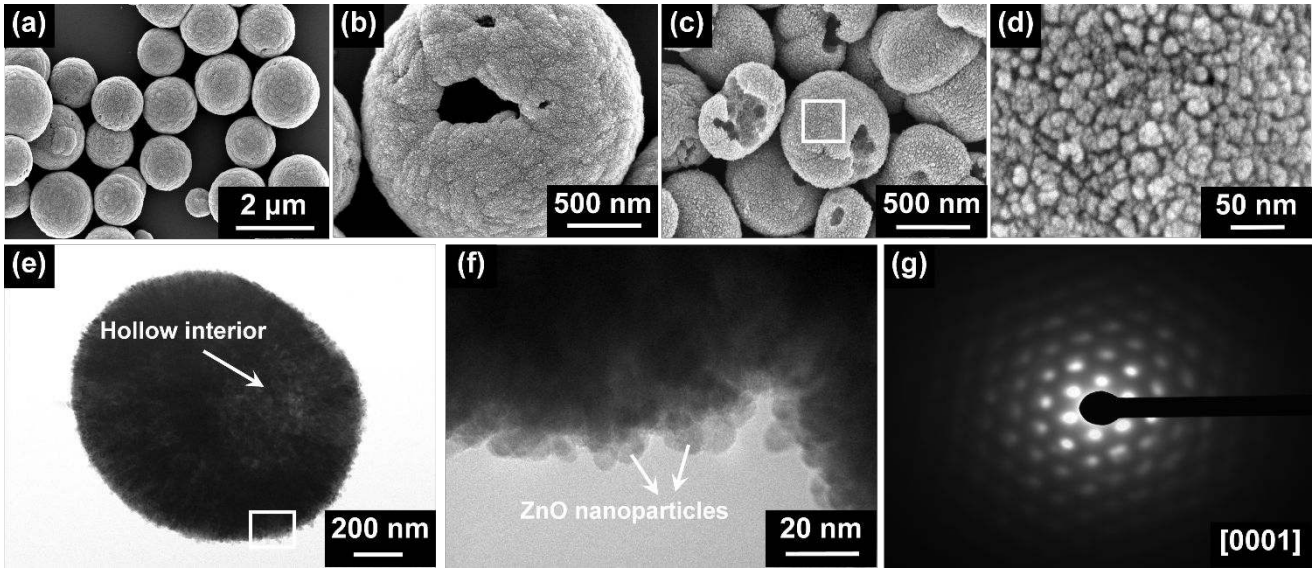

Figure 3. SEM images of the ZnO product obtained using the anthocyanin-assisted solvothermal reaction before (a, b) and after calcination in air at 350 °C for 2 h (c, d). TEM images of a single calcined hollow ZnO sphere (e) and its constituent nanoparticles (f). (g) Selected area electron diffraction (SAED) pattern of a single calcined ZnO hollow sphere from [0001] direction.

SEM images of the ZnO product obtained from the anthocyanin-assisted solvothermal reaction are given in **Figure 3a-d**. The addition of anthocyanin during the solvothermal reaction leads to the formation of ZnO spheres with inner cavities (*i,e.*, ZnO hollow spheres). The diameters of these spheres vary from ~1 to 2 μm (**Figure 3a, b**). Anthocyanin plays a crucial role in the formation of the ZnO hollow spheres because in the absence of anthocyanin, the resulting ZnO product exhibits a hemisphere-like morphology. The shrinkage of the ZnO hollow spheres is observed after calcination with the average size of the calcined ZnO spheres being 1 μm, roughly half of that of the non-calcined spheres. The size shrinkage is likely to originate from the decomposition of anthocyanin and its by-products. From the high-magnification SEM images in **Figure 3c, d**, it is clear that these spheres are assembled by small nanoparticles. The hollow nature of the calcined ZnO product is confirmed by the TEM image shown in **Figure 3e**. **Figure 3f** reveals that the as-prepared ZnO hollow spheres are constructed by nanoparticles with sizes between 8 to 15 nm, which are smaller than the calculated crystallite size. Moreover, the selected area electron diffraction (SAED) pattern of a single calcined hollow ZnO sphere (**Figure 3g**) reveals the preferred crystal growth along the direction perpendicular to the

<0001> direction. It has been reported that the polar (0001) plane could provide more active sites for gas adsorption due to the high abundance of oxygen vacancies.[25, 77]

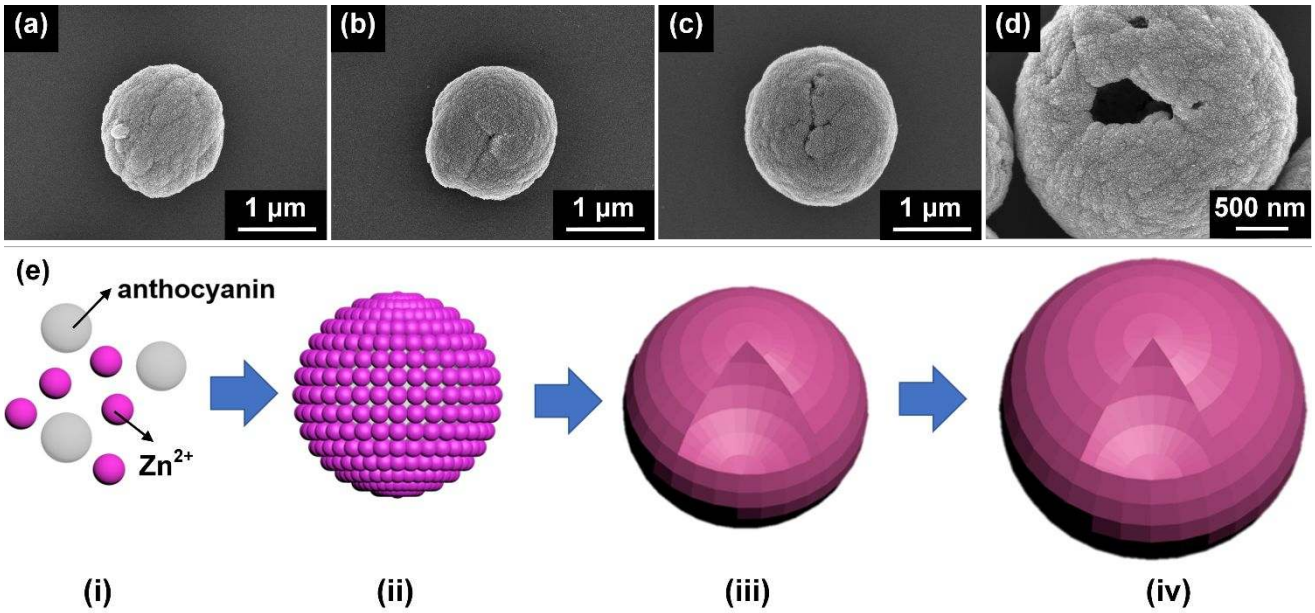

Figure 4. SEM images of the products obtained after 2 h (a), 4 h (b), 8 h (c), and 16 h (d) of solvothermal reaction in the presence of anthocyanin. (e) Schematic illustration depicting the growth mechanism of ZnO hollow spheres in the presence of anthocyanin.

To investigate the effect of anthocyanin on the morphology of the ZnO product, different amounts of the gel-like anthocyanin (0.0103, 0.0206, and 0.0352 g) were used during the solvothermal reaction. In the absence of anthocyanin, the resulting ZnO product shows an aggregated hemisphere-like morphology which is assembled of tiny rod-like particles (**Figure S3a, b**). Anthocyanin is observed to promote the formation of spherical particles which are assembled of smaller nanoparticles and the addition of an optimum amount of anthocyanin (0.0103 g) leads to the generation of well-defined hollow spheres (**Figure S3c, d**). However, the use of excess anthocyanin leads to the collapse of these spheres which are undesirable for gas-sensing applications (**Figure S3e-h**). Furthermore, the effect of reaction time was also investigated to understand the formation mechanism of these hollow spheres. As presented in **Figure 4a**, sphere-like particles are readily formed within 2 h of solvothermal reaction. The increase of reaction time basically increases the average diameter of the spheres and promotes the formation of cavities on these spheres (**Figure 4b-d**). The spheres obtained after 2 h have an average diameter of 1.5 μm, which increases to 1.7 μm, 2 μm, and 2.2 μm after 4

h, 8 h, and 16 h of reaction, respectively. It is clear that Ostwald ripening is responsible for the size increment of these spheres. Based on the above observations, the following formation mechanism is proposed. The low solubility of anthocyanin in 2-propanol indicates the higher polarity of anthocyanin relative to 2-propanol. This difference in solubility leads to the formation of microemulsion of anthocyanin in 2-propanol system (**Figure 4e (i)**). The aggregated microemulsion acts as a soft template for the growth of ZnO (**Figure 4e (ii)**). Under the solvothermal condition at 180 °C, anthocyanin becomes unstable and decomposed into smaller compounds[78], and leaves behind cavities inside these spheres (**Figure 4e (iii)**). As the reaction time increases, further growth of ZnO takes place, leading to the increase of diameter (**Figure 4e (iv)**). This formation mechanism is schematically illustrated in **Figure 4e**.

SEM images of the ZnO-MWCNT composites obtained with different atomic ratios of ZnO and MWCNTs are presented in **Figure 5a-f**. The pristine MWCNTs exhibit diameters in the range of 20-40 nm and the morphology remains identical after the acid treatment, as evident in **Figure S4a, b**. In the case of the ZnO-MWCNT (15:1) composite, many cavities are seen on the ZnO spheres following the modification with MWCNTs. Based on the TEM analysis, the average size of the cavities on the ZnO hollow spheres is around 500 nm, which is significantly larger than the average diameter of the MWCNTs (30 nm). As a result, at this optimum ZnO/MWCNT ratio, many MWCNTs are able to penetrate into the cavities of these spheres, providing good interconnection between the hollow spheres, which is useful for enhancing the electron transport. At a ZnO:MWCNT ratio of 10:1, more cavities are formed on the ZnO spheres and some MWCNTs are observed to penetrate into these cavities. With a further decrease in the ZnO:MWCNT ratio to 5:1, many of the ZnO spheres become partially broken and the MWCNTs are unable to enter the cavities of these spheres and instead exist separately. Furthermore, at this ratio, the surface roughness of the ZnO spheres appears to be enhanced due to the increase in the density of the assembling nanoparticles on MWCNTs.

Functional groups present on the surface of MWCNTs, such as hydroxyl (-OH) and carboxyl groups (-COOH) as a result of the acid treatment provides favorable sites for the nucleation and growth of ZnO nanoparticles. In this case, a strong interaction occurs between the -OH group on ZnO and carboxylic group on functionalized MWCNT and the binding between the two groups is facilitated *via* esterification.[79] The TEM images of ZnO-MWCNT composites with low (15:1) and high amounts of MWCNTs (5:1) are shown

in **Figure S5a, b**. In agreement with the SEM observations, the surface roughness of the ZnO spheres appears to increase with the increased amount of MWCNTs. The growth of ZnO nanoparticle on the surface of the MWCNT at a low ZnO:MWCNT ratio of 5:1 is observed from the HRTEM image shown in **Figure S5c**. The multilayered nature of the CNTs is confirmed by the presence of several layers rolled up together along the the same axis, as seen in **Figure S5d**.

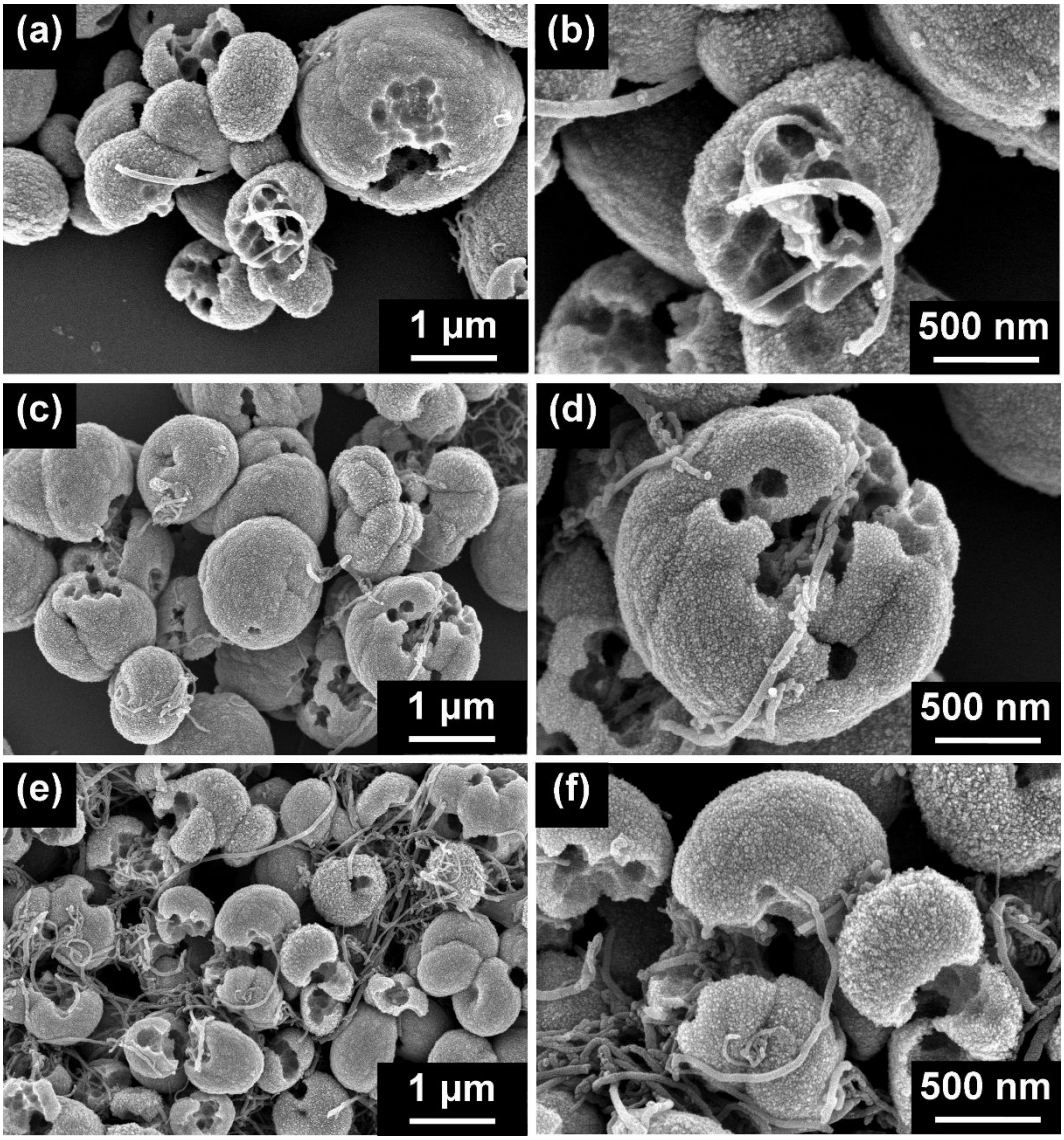

Figure 5. Low- and high-magnification SEM images of ZnO-MWCNT composites with ZnO/MWCNT ratios of 15:1 (a, b), 10:1 (c, d), and 5:1 (e, f).

To estimate the band gaps of the pristine ZnO and ZnO-MWCNT composites, optical characterizations by UV-visible spectroscopy were carried out. As shown in **Figure S6a**, the ZnO hollow spheres exhibit a peak at 367 nm which is red-shifted to 371 nm, 378 nm, and 381 nm for ZnO-MWCNT (15:1), (10:1), and (5:1)

composites, respectively. From the Tauc's plots (**Figure S6b**), the optical band gaps of pure ZnO and ZnO-MWCNT (15:1), (10:1), and (5:1) composites are estimated to be 2.9 eV, 2.8 eV, 2.6 eV and 2.3 eV, respectively. This trend indicates that the addition of MWCNTs to the ZnO enriches the charge carrier and leads to the band gap contraction of ZnO.[80-81]

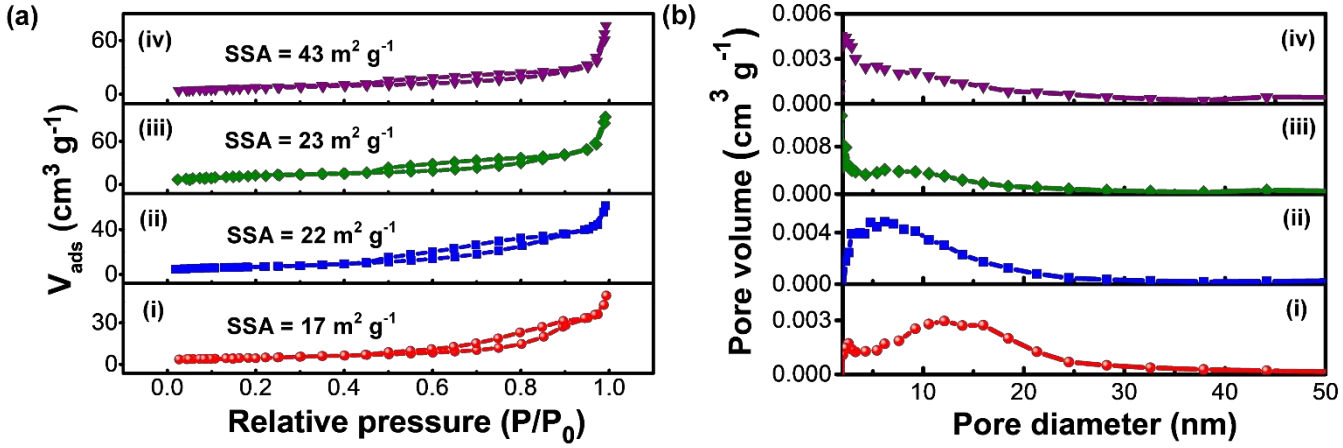

Figure 6. Nitrogen adsorption-desorption isotherms (a) and pore size distribution plots (b) of ZnO hollow spheres (i) and ZnO-MWCNT (15:1) (ii), (10:1) (iii), and (5:1) (iv) composites.

Nitrogen adsorption-desorption isotherms and pore size distribution curves of the pure ZnO and ZnO-MWCNT composites are given in **Figure 6**. The presence of hysteresis loops in the isotherms implies the hollow nature of ZnO in all samples. BET method was used to estimate the specific surface areas of the samples. The pristine ZnO hollow spheres have a relatively low specific surface area of 17 $m^2 g^{-1}$ and exhibit mostly mesopores (pore size between 2-50 nm) with some macropores (pore size > 50 nm) (**Figure 6a (i)**). In comparison, the BET specific surface areas are 22 $m^2 g^{-1}$, 23 $m^2 g^{-1}$, and 43 $m^2 g^{-1}$ for ZnO-MWCNT composites with ZnO/MWCNT ratios of 15:1, 10:1, and 5:1, respectively (**Figure 6a (ii-iv)**). The increase in surface area is attributed to the large surface area of the MWCNTs, which is 148 $m^2 g^{-1}$ (**Figure S7**). Furthermore, increasing the amount of MWCNTs appears to slightly narrow the pore size of the resulting composite (**Figure 6b (i-iv)**), thereby leading to the small increment in surface area.

3.2. Gas-sensing properties

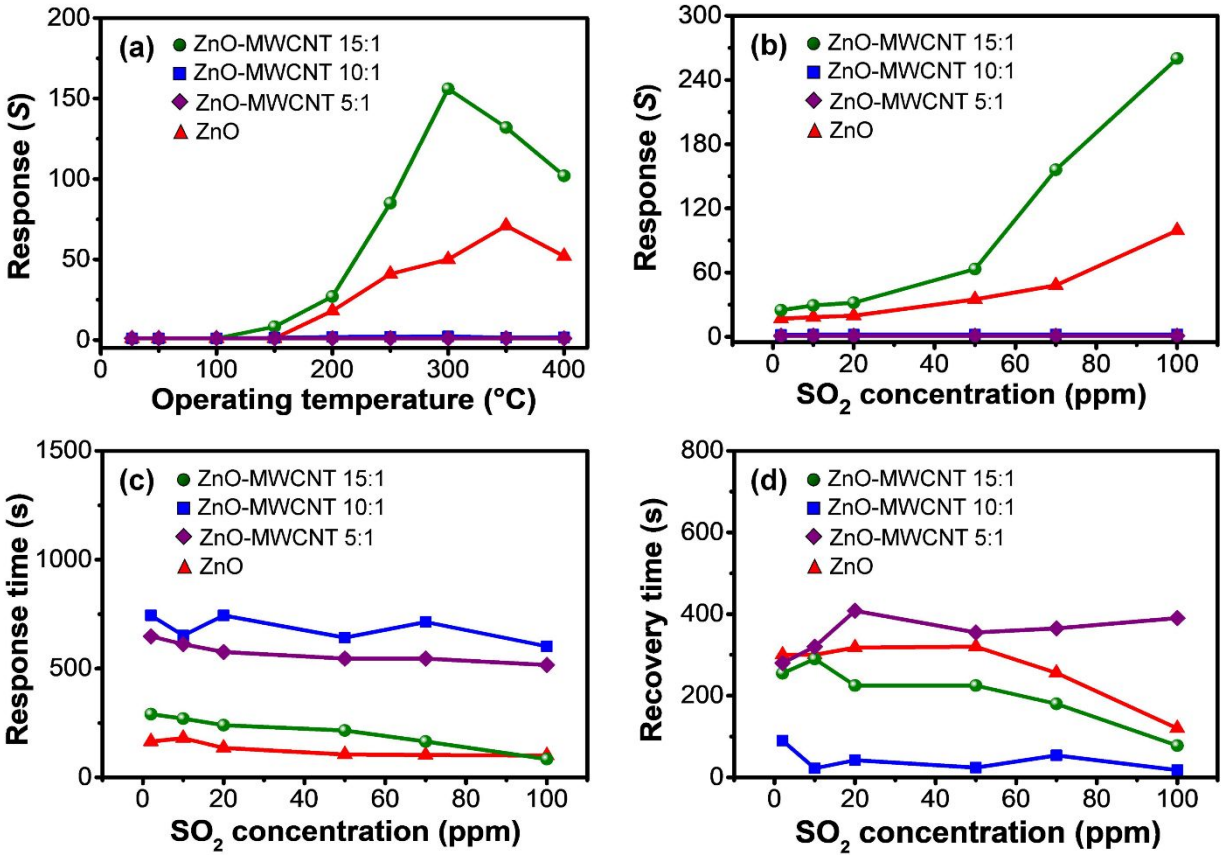

Figure 7. (a) Response *versus* temperature plots for ZnO hollow spheres and ZnO-MWCNT (15:1, 10:1, and 5:1) composites towards 70 ppm of SO_2 gas. (b) Response *versus* concentration plots for ZnO hollow spheres and ZnO-MWCNT (15:1, 10:1, and 5:1) composites at 300 °C. Response times (c) and recovery times (d) of all prepared sensors on exposure to various concentrations of SO_2 gas at 300 °C.

The main purpose of adding MWCNTs to ZnO hollow spheres is to lower the operating temperature and reduce power consumption, while also enhancing their gas-sensing performance. In this work, different ratios of ZnO:MWCNT were selected to investigate the influence of the addition of MWCNTs on the sensing behavior, sensitivity, selectivity, and response-recovery properties of the ZnO hollow spheres. The operating temperature is one of the most important parameters affecting the mobility of electrons and hence, the conductivity of the material. As such, gas-sensing measurements were carried out at various temperatures from 27 to 400 °C and the responses of the pristine ZnO and ZnO-MWCNT composite sensors with increasing operating temperature are shown in **Figure 7a**. From **Figure 7a**, it is clear that the incorporation of MWCNTs leads to lowering of the optimum operating temperature. In the case of pure ZnO, it starts to detect 70 ppm of

SO_2 at 200 °C with a response (*S*) value of 18. In the case of ZnO-MWCNT (15:1) and (10:1) composites, they start to detect SO_2 gas at 150 °C with response values of 8 and 1.3, respectively. In general, the responses of these sensors gradually increase with increasing temperature up to the optimum temperature, before decreasing as the temperature is increased beyond the optimum temperature. Thermal energy is required to activate the surface reaction between oxygen and SO_2 and the optimum temperature is achieved when the adsorption rate is equal to the desorption rate.[82] Beyond the optimum temperature, the desorption rate is higher than the adsorption rate and causes a decrease in the response. The pristine ZnO hollow spheres exhibit *S* values of 18, 41, 50, 71, and 52 at 200, 250, 300, 350, and 400 °C, respectively. In comparison, the ZnO-MWCNT (15:1) composite shows very high *S* values of 8.2, 27, 85, 156, 132, and 102 towards 70 ppm of SO_2 gas at 150, 200, 250, 300, 350, and 400 °C, respectively. However, the ZnO-MWCNT (10:1) composite gives low *S* values of 1.3, 1.8, 1.9, 2.2, 1.6, and 1.4 towards 70 ppm of SO_2 gas at 150, 200, 250, 300, 350, and 400 °C, respectively.

Further, the ZnO-MWCNT (5:1) composite shows a small response of 1.030 at room temperature. This value decreases to 1.020, 1.015, and 1.010 as the temperature increases to 50, 100, and 150 °C, respectively. However, the response value increases again to 1.017 and 1.030 at 200 and 300 °C, respectively , but decreases to 1.01 at 400 °C. It is clear that different interactions occur at different temperatures. At low temperatures (RT-150 °C), physical adsorption occurs *via* Van der waals interactions. The increase of temperature leads to the rise in entropy, which decreases the sensing response. At higher temperatures (150-400 °C), thermally-activated chemisorption process takes place that involves the adsorption of oxygen ions. A similar phenomenon has been observed in our previous work.[83] From the above results, it is obvious that the ZnO:MWCNT ratio has a profound influence on the sensing response to SO_2. At all temperatures, the incorporation of a very small amount of MWCNTs to ZnO (ZnO:MWCNT = 15:1) can greatly enhance its sensing response, especially at 300 °C, where the response is increased by nearly three-fold from 50 to 156, compared to that of pure ZnO. In this case, the synergistic effect between MWCNTs (*p*-type sensing material) and ZnO (*n*-type sensing material) and the formation of the *p*-*n* heterojunction are believed to be responsible for the enhanced sensitivity. The presence of a *p*-*n* heterojunction leads to an additional potential barrier, as proven by the calculated activation energy. Using the Arrhenius equation, the activation energy of the ZnO-

MWCNT (15:1) composite is determined to be 0.24 eV, which is higher than that of pure ZnO hollow spheres (0.21 eV) (**Figure S8**). Moreover, the presence of the *p-n* heterojunction does not only generate additional barrier potential but also increases the chemisorption of oxygen molecules.[6, 84-86] As a result, the change in resistance of the ZnO-MWCNT (15:1) composite upon exposure to SO_2 gas is higher than that of ZnO hollow spheres.

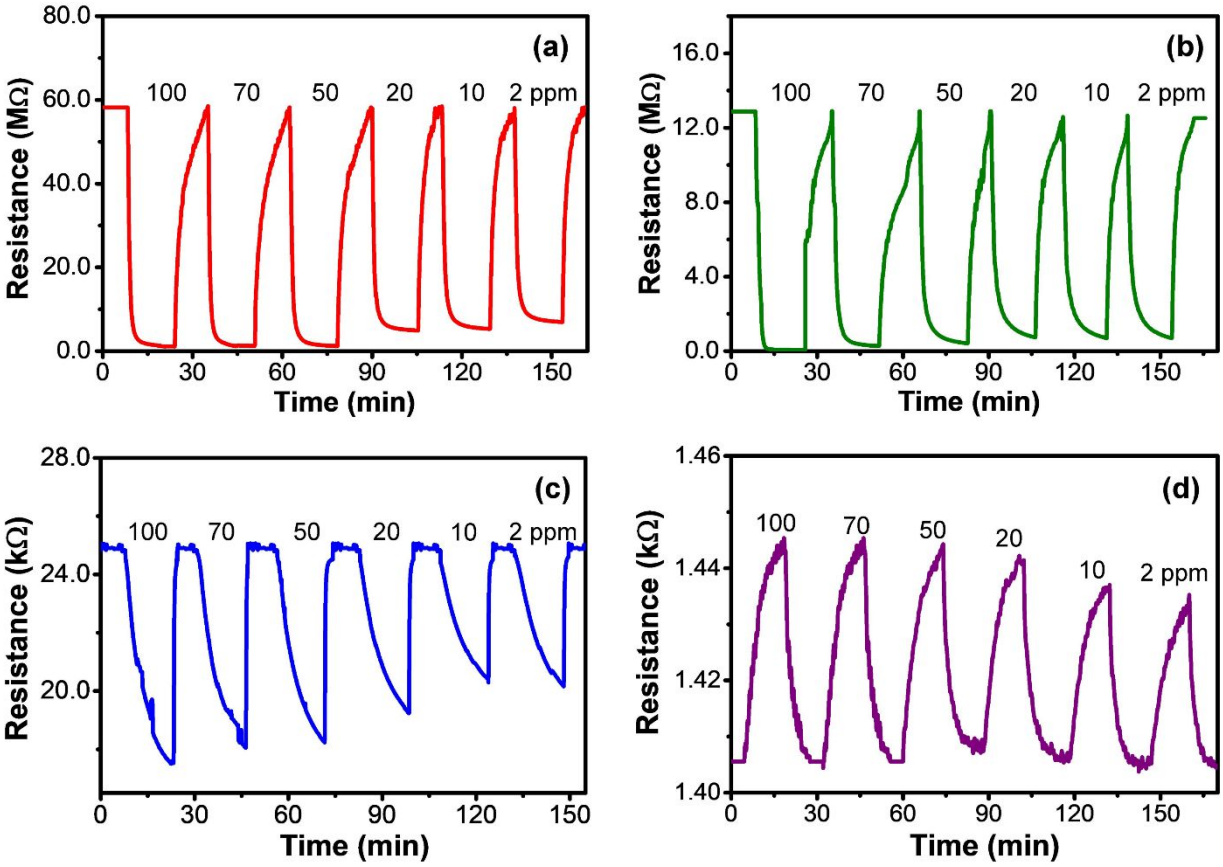

Figure 8. Dynamic response-recovery curves of ZnO (a) and ZnO-MWCNT composites with ZnO:MWCNT ratios of 15:1 (b), 10:1 (c), and 5:1 (d) towards 2, 10, 20, 50, 70, and 100 ppm of SO_2 gas at 300 °C.

The responses of pure ZnO and ZnO-MWNCT composites towards various concentrations of SO_2 gas are depicted in **Figure 7b**. The pristine ZnO hollow spheres exhibit responses of 16.9, 18.3, 19.7, 34.9, 48.0, and 99.4 to 2, 10, 20, 50, 70, and 100 ppm of SO_2, respectively. In comparison, MWCNTs show some response to SO_2 gas at low temperatures, however at high temperatures they show even lower response values, indicating that alone, they are not suitable for high-temperature sensors. Compared to both ZnO and MWCNTs, the ZnO-MWCNT (15:1) composite displays higher responses of 24.8, 29.4, 31.8, 63.3, 156, and 260 towards 2, 10, 20, 50, 70, and 100 ppm of SO_2, respectively. Meanwhile, the responses of the ZnO-

MWCNT (10:1) composite towards identical concentrations of SO_2 gas are 1.88, 1.92, 2.02, 2.12, 2.14, and 2.21, respectively. With the exception pure MWCNTs, the ZnO-MWCNT (5:1) composite shows the lowest sensing performance as its response barely changes with the increase of SO_2 concentration. It is important to note that the gas-sensing results shown in **Figure 7** were obtained at a fixed humidity level of 65%. In order to check the effect of humidity, the response of the optimum sensor (*i.e.*, ZnO-MWCNT (15:1) composite) towards SO_2 gas was also investigated at a higher humidity level of 80%. The response of this composite towards 70 ppm of SO_2 at 300 °C decreases from 156 to 127 with the increase of humidity level from 65% to 80%. This is because the increased presence of moisture on the surface of the ZnO-MWCNT composite sensor at a higher humidity level can reduce the amount of SO_2 molecules adsorbed on its surface.[27]

For comparison, two control samples have been prepared, including ZnO solid spheres prepared with ethylene glycol (EG) and ZnO-MWCNT (15:1) composite prepared without anthocyanin (*Figure S9*). As seen in **Figure S9a**, the ZnO product synthesized in the presence of ethylene glycol (instead of anthocyanin) displays solid spherical morphology with large diameters between 1.5-2.5 μm and smoother surface. As shown in **Figure 7a**, the ZnO hollow spheres readily give response to SO_2 gas at temperatures as low as 200 °C. In contrast, the sensor based on ZnO solid spheres does not show any response to SO_2 gas at the same temperature due to its high resistance (>100 MΩ). In fact, they only start to show a response to SO_2 gas at 400 °C with a response value of 210. This response is higher than that of ZnO hollow spheres at its optimum temperature (*S* = 156 at 300 C). However, such a high working temperature is not beneficial for practical sensing applications as it will lead to high power consumption and reduced lifetime. The above results imply that the hollow architecture is beneficial for lowering the working temperature of the ZnO sensor. The ZnO-MWCNT (15:1) composite prepared without anthocyanin has an irregular morphology and size of more than 2 μm and no penetration of MWCNTs is observed, as seen in **Figure S9b**. When employed for SO_2 sensing, the composite prepared without anthocyanin displays a response of 72 to 70 ppm SO_2 at 300 °C, which is only roughly half of that of the ZnO-MWCNT (15:1) composite prepared with anthocyanin (**Figure S9c**).

A comparison of the SO_2 sensing performance of the optimum ZnO-MWCNT (15:1) composite against previously reported metal oxide-based sensors is given in **Table S1**. From this Table, it can be observed that the ZnO-MWCNT (15:1) composite displays a much higher sensing performance towards SO_2 gas than

previous sensors based on CuO nanoplates[87], ZnO nanoflowers[88], SnO_2 nano-dodecahedrons[89], $BiFeO_3$ and WO_3 nanoparticles[90-91], and NiO-ZnO composites[92-93], despite exhibiting slightly to moderately higher optimum operating temperature. For instance, CuO nanoplates displayed a response of 2.80 to 10 ppm of SO_2 gas at 200 °C.[87] This value is considerably lower than that of the ZnO-MWCNT (15:1) composite, which shows a 10 times higher response (S = 29.4) to 10 ppm of SO_2 at the same temperature. Moreover, at optimal operating temperature of 300 °C, our composite shows a higher response of 24.8 to 2 ppm of SO_2 compared to $BiFeO_3$ nanoparticles which showed a response of 2.03 to 5 ppm of SO_2. Furthermore, the ZnO-MWCNT (15:1) composite also displays a response of 85 to 70 ppm of SO_2 gas at 250 °C, which is higher the responses towards 100 ppm of SO_2 gas for ZnO nanoflowers (S = 30.4) at 260 °C and ZnO nanodisks (S ~50) at 240 °C.[92-93] Furthermore, our composite also displays comparable sensing performance to NiO-decorated ZnO nanoflowers which showed a response of 84.2 to 100 ppm of SO_2 gas at 220 °C.[92] The relatively higher performance of ZnO hollow sphere-MWCNT (15:1) results from a combination of the hollow structure and the *p-n* heterojunction formed at the ZnO/MWCNT interface.

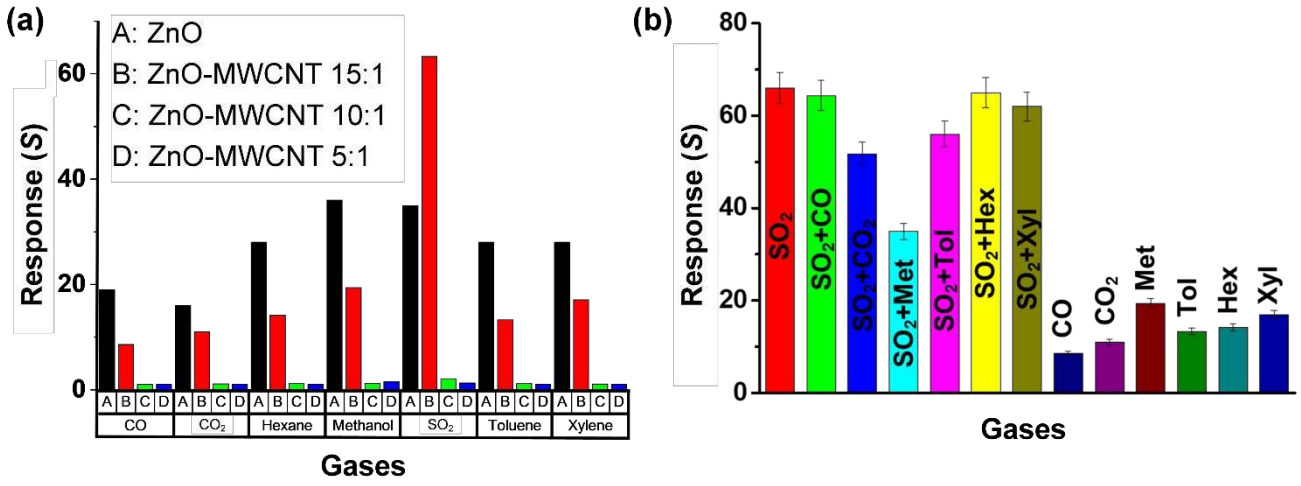

Figure 9. (a) Individual selectivity tests of pristine ZnO hollow spheres and ZnO-MWCNT (15:1), (10:1), and (5:1) composites towards 50 ppm of SO_2 gas at 300 °C. (b) Responses of the ZnO-MWCNT (15:1) composite towards pure SO_2 gas (50 ppm) and SO_2 gas in the presence of various interfering gases (the concentration of the interfering gas is also 50 ppm) at 300 °C.

The response and recovery times of all sensors towards various concentrations of SO_2 are given in **Figure 7c, d**. The response time is defined as the time needed for the sensor to reach 90% of steady state after exposure

to the gas. The response time basically increases as the amount of MWCNT increases to the ratio of 10:1 and decreases with this ratio lowered to 5:1. At SO_2 concentrations of 2, 10, 20, 50, 70, and 100 ppm, the response times of the pristine ZnO sensor are 165, 180,135, 105, 103, and 100 s, respectively, whereas the response times of ZnO-MWCNT (15:1) composite are 290, 270, 240, 215, 165, and 84 s, respectively. The response times for ZnO-MWCNT (10:1) composite are 744, 652, 744,642, 714, and 602 s, respectively, while for the ZnO-MWCNT (5:1) composite, the response times are 648, 612, 576, 546, 546, and 516 s, respectively. These results indicate that the addition of MWCNTs prolongs the response time, however the extension in the response time can be minimized by using low amounts of MWCNTs, as seen in the case of the ZnO-MWCNT (15:1) composite. The recovery time is defined as the time required for the sensor to reach 10% from the baseline after removal of the gas. The recovery times of the pristine ZnO sensor towards 2, 10, 20, 50, 70, and 100 ppm of SO_2 are 300, 300, 318, 320, 256, and 120 s respectively, for ZnO-MWCNT 15:1 255, 290, 225, 225, 180, and 78 s respectively, for ZnO-MWCNT 10:1 are 90, 22, 42, 24, 54, and 18 s respectively, while for ZnO-MWCNT 5:1 are 280, 320, 408, 355, 365, and 390 s, respectively. These results reveal that addition of low contents of MWCNTs is beneficial for achieving faster recovery time.

The lower sensing responses of ZnO-MWCNT (10:1) and (5:1) composites may be attributed to two main reasons. At lower ZnO:MWCNT ratios, the sensing contribution of MWCNTs becomes dominant, and while MWCNTs typically excel at lower operating temperatures (<100 ^oC), they tend to exhibit poorer sensing performance at higher temperatures. Unlike pristine ZnO and ZnO-MWCNT (15:1) and (10:1) sensors which display *n*-type sensing behaviors (*i.e.,* the resistance decreases when exposed to SO_2 gas) as seen in **Figure 8a-c**, the ZnO-MWCNT (5:1) composite instead displays a *p*-type sensing behavior, in which the resistance increases upon exposure to SO_2, as shown in **Figure 8d**. The change in sensing behavior from *n*-type to *p*-type is evident and further supports the dominant sensing contribution of MWCNTs in this composite. Another possible reason is that at the lower ZnO:MWCNT ratios, many ZnO hollow spheres become broken and the majority of the MWCNTs cannot enter the cavities of the spheres; rather they exist separately, and this leads to poor interconnectivity between the particles. Moreover, the dominant role of MWCNTs in determining the electrical properties of the two composites is also responsible for their poorer sensing performance at high temperatures. The activation energies are calculated to be 0.17 and 0.06 eV for ZnO-MWCNT (10:1) and (5:1)

composites, respectively. The decrease in activation energy with increasing MWCNT content is due to the low activation energy of MWCNT (0.01 eV).

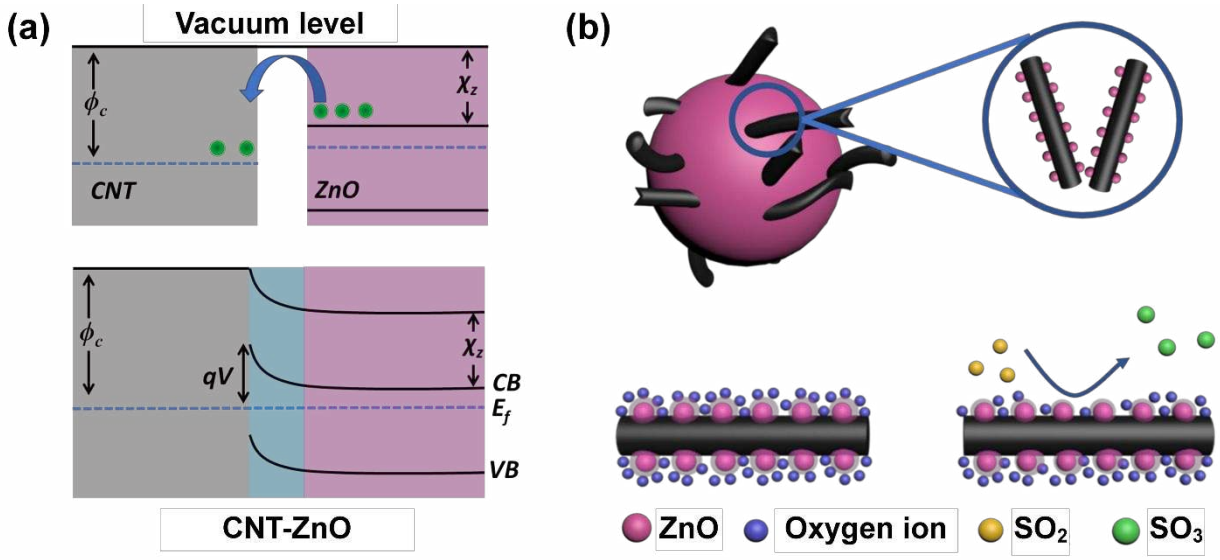

Figure 10. (a) Schematic illustration showing the band diagram of the ZnO-MWCNT composite. (b) Schematic diagram depicting the SO_2 sensing mechanism of ZnO-MWCNT composite.

To investigate the ability of these sensors to distinguish SO_2 in the presence of other gases, they were exposed to 50 ppm of six different gases, including CO, CO_2, methanol, toluene, hexane, and xylene. These gases were selected as SO_2 gas may be generated together with CO, CO_2, and other VOCs in fuel combustion in power plants, wood treatment plants, and chemical industries.[94-95] Comparison of the responses of all sensors to the above seven gases, including SO_2, is presented in **Figure 9a**. The pristine ZnO sensor shows its highest response towards methanol, while also displaying cross-sensitivity to other gases. It is clear that the addition of a small amount of MWCNTs in the sample with a ratio of 15:1 can greatly enhance the selectivity towards SO_2. On the other hand, both ZnO-MWCNT (10:1) and (5:1) composites exhibit poor selectivity towards SO_2. These results suggest that the optimum ZnO:MWCNT ratio for achieving both high sensitivity and selectivity towards SO_2 is 15:1. The enhancement in the selectivity of the ZnO-MWCNT (15:1) composite towards SO_2 gas may be attributed to the presence of oxygen functional groups on the surface of the MWCNTs, such as hydroxyl and carbonyl groups that may promote the adsorption and selectively bind SO_2.[96-97] Moreover, we have also performed cross selectivity test for the optimum sensor (ZnO-MWNCT (15:1) composite), where the SO_2 gas was injected simultaneously with each interfering gas, similar to that used in

a previous report.[98] **Figure 9b** displays the cross-selectivity or comparison between the responses of the ZnO-MWCNT (15:1) composite to pure SO_2 gas and SO_2 gas in the presence of other interfering gases. The response values of this composite to SO_2 gas in the presence of CO and hexane are almost identical to the response value to pure SO_2 gas. Furthermore, the response values of the ZnO-MWCNT (15:1) composite to SO_2 gas in the presence of CO_2 and toluene are only slightly lower than the response value to pure SO_2 gas. These results imply the good selectivity of this composite sensor to SO_2 against CO, CO_2, toluene, and hexane. The lowest response is observed when the SO_2 gas was mixed with methanol, suggesting that this composite sensor may not be able to distinguish between SO_2 gas and methanol effectively.

As a gas-sensing material, the electrical properties of ZnO are strongly affected by the chemical environment, especially oxygen adsorption. It is well-known that oxygen species in air can adsorb on the surface of ZnO, and dissociates and ionizes to different states of oxygen ions depending on the operating temperature.[1, 99-101] Below 100 °C, the ZnO surface is dominated by O_2^-species and between 100-300 °C, the number of O_2^- species is reduced and O^- species become dominant, while above 300 °C, the surface of ZnO is dominated by O^{2-} species. The formation of ionic oxygen species can be expressed as follows[102]:

$$O_2\,(gas) \Leftrightarrow O_2\,(ads) \tag{4}$$

$$O_2\,(ads) + e^- \Leftrightarrow O_2^-\,(ads) \tag{5}$$

$$O_2^-\,(ads) + e^- \Leftrightarrow 2O^-\,(ads) \tag{6}$$

$$O^- + e^- \Leftrightarrow O^{2-}\,(ads) \tag{7}$$

The adsorption of oxygen ions generates an electron depletion layer on the surface of ZnO, which leads to the increase of its resistance. At nanoscale, the sensing mechanism is mainly contributed by the change in the width of the depletion layer. When the surface of the ZnO sensor is exposed to SO_2, the SO_2 gas will react with the oxygen ion species and becomes converted to SO_3 by releasing electrons to the surface and narrowing the depletion layer, which leads to the decrease in resistance. This reaction can be expressed by the equation:

$$SO_2 + O^{2-}\,(ads) \rightarrow SO_3 + 2e^- \tag{8}$$

In the case of ZnO-MWCNT composites, there are three main mechanisms. First, on the surface of ZnO spheres in the composites, a similar mechanism occurs as that in the case of pure ZnO sensor as described above. Second, at the interface of ZnO and MWCNTs, a *p-n* heterojunction is formed. The smaller band gap

of MWCNT (~0.05-2.0 eV) compared to that of ZnO (2.9 eV for ZnO hollow spheres) results in the band diagram modification to a metal/semiconductor band diagram (**Figure 10a**). As the *p-n* heterojunction is formed, the different work function between MWCNTs and ZnO and the electron affinity of ZnO promote the transfer of electrons from ZnO to MWCNTs and holes from MWCNTs to ZnO. The transfer of these charge carriers creates a space charge region at the ZnO/MWCNT interface which generates a built-in potential which changes in the presence of SO_2 gas.

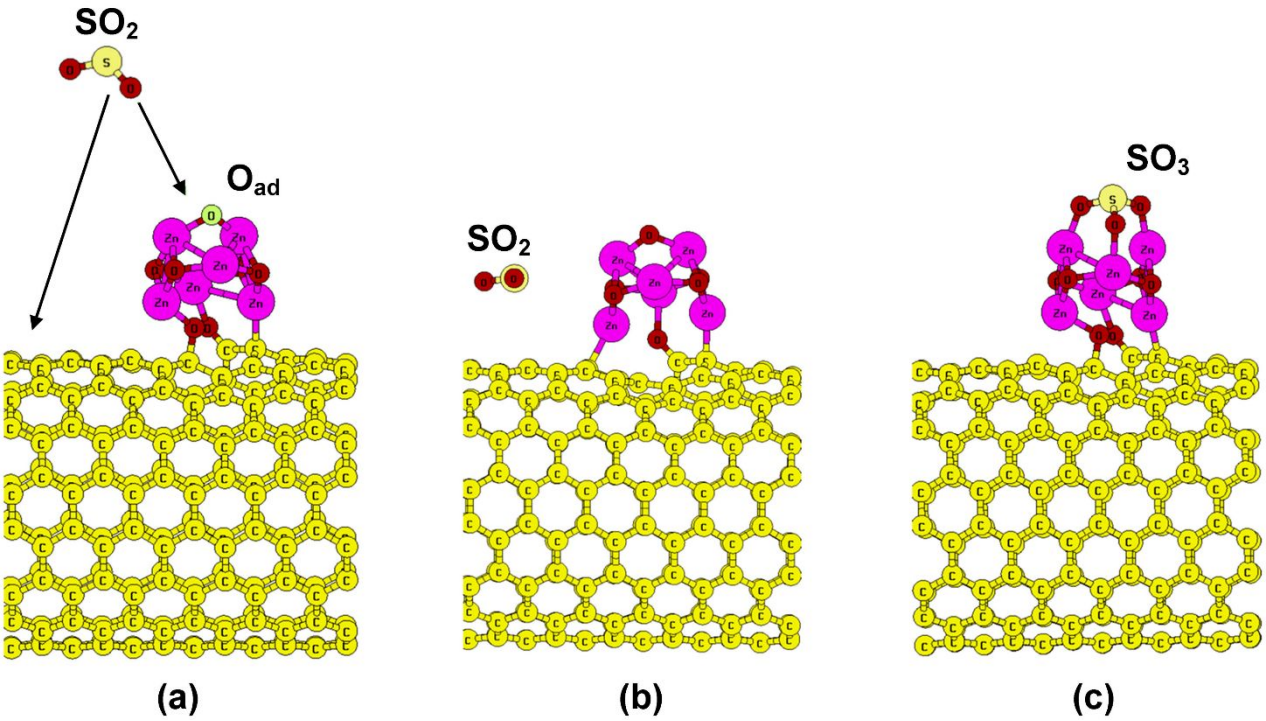

Figure 11. (a) Initial structure of SO_2 interaction with $CNT^{[MV]}/Zn_6O_6$ system. The O adatom is labeled as O_{ad}. (b) SO_2 physisorption on the C-C cite of CNT. (c) SO_2 adsorption on the $CNT^{[MV]}/Zn_6O_6$ with an O adatom.

The third mechanism is related to the surface of MWCNT which exhibits the characteristics of a *p*-type semiconductor. The sensing mechanism of the ZnO-MWCNT composite is illustrated in **Figure 10b**. In contrast to ZnO, the adsorption of oxygen ions causes the formation of hole accumulation layer on MWCNTs, which lowers their resistance. Upon introduction of SO_2, the oxygen ions (most likely O^{2-} at 300 °C) adsorbed on the surface of the MWCNTs react with the SO_2 gas form SO_3 by releasing electrons to the surface (Eq. 8). The recombination of electrons and holes occurs, leading to the narrowing of the hole accumulation layer and the increase in resistance. The proposed sensing mechanism in **Figure 10b** is supported by previous studies

on metal oxide/CNT composite sensors.[1, 84-85] The dynamic response-recovery curves of the pure MWCNT sensor to 70 ppm of SO_2 at 300 °C are given in **Figure S10**. For the ZnO-MWCNT (15:1) composite, the built-in potential formed at the ZnO/MWCNT interface can enhance the change in resistance of the composite sensor upon the trapping of electrons, thereby leading to a higher sensing response towards SO_2.[103] The much higher proportion of ZnO than MWCNTs in this composite leads to the first and second mechanisms to be the dominant mechanisms and the generation of *n*-type sensing behavior. For the ZnO-MWCNT (10:1) composite, there is a competing mechanism between the first and the third mechanisms, however, the first mechanism still prevails over the third one due to the higher proportion of ZnO in this particular composite, leading to the *n*-type sensing behavior. On the other hand, for the ZnO-MWCNT (5:1) composite, the third mechanism is the dominant one, largely due to the high concentration of MWCNTs in this composite. This consequently leads to the *p*-type sensing behavior of the ZnO-MWCNT (5:1) composite.

To model reaction (8), we performed DFT calculations for SO_2 adsorption on the surface of $CNT^{[MV]}/Zn_6O_6$ with the presence of an O adatom on the Zn_6O_6 cluster. This model was adapted from previous references.[63-64, 104] SO_2 molecule can only be adsorbed on the Zn_6O_6 cluster and not on the bare CNT surface. The SO_2 molecule is only physically adsorbed on the C-C site of the CNT with a weak adsorption energy of -0.03 eV. The most stable SO_2 adsorption is found when the SO_2 molecule is adsorbed on the proximity of the O adatom with a strong adsorption energy (-2.00 eV), as shown in **Figure 11**. The optimization results show that the incoming SO_2 molecule directly interacts with the O adatom of Zn_6O_6 to form SO_3 molecule, in agreement with Eq. 8. The adsorbed SO_2 molecule donates its charge of about 0.46 e to the $CNT^{[MV]}/Zn_6O_6$ system (0.12 e to the Zn_6O_6 and 0.36 e to the CNT) during the surface reaction. SO_3 is often considered as an adsorbed gas that can be easily desorbed from the surface. The existence of charge transfer from ZnO to CNT implies the presence of a potential barrier at the $CNT^{[MV]}/Zn_6O_6$ interface. This suggests that the CNT indeed acts as an electron conduction channel in the ZnO/CNT composite.

4. Conclusions

This study demonstrates the first utilization of anthocyanin extracted from black rice (*Oryza sativa L.*) grains as a structure-directing agent to promote the formation of ZnO hollow spheres which are constructed by the

self-assembly of small nanoparticles. The modification of these spheres with the optimum amount of MWCNTs leads to the creation of many cavities on the ZnO spheres. This in turn, allows the MWCNTs to penetrate into the interior of these spheres, thereby creating good interconnectivity between the particles and smooth pathway for electron transport. However, the excess addition of MWCNTs is not preferable as it leads to the structural breakdown of the ZnO hollow spheres. When tested for SO_2 sensing, the ZnO-MWCNT (15:1) composite shows superior sensing performance compared to pristine ZnO and ZnO-MWCNT (10:1) and (5:1) composites. This optimum composite displays a high sensing response of 156 to 70 ppm of SO_2 gas at 300 °C, which is more than thrice that of pure ZnO sensor. Furthermore, the ZnO-MWCNT (15:1) composite also shows good selectivity to SO_2 gas compared to other gases, such as CO, CO_2, methanol, toluene, hexane, and xylene, with relatively low cross-selectivity. The additional potential barrier generated by the creation of a *p*-*n* heterojunction at the interface of ZnO/MWCNT leads to a greater change in the resistance of the ZnO-MWCNT (15:1) composite upon exposure to SO_2 gas relative the pure ZnO sensor. Interestingly, the sensing behavior of the composite strongly depends on the amount of MWCNT in the composite. ZnO-MWCNT composites with ZnO/MWCNT ratios of 15:1 and 10:1 exhibit an *n*-type sensing behavior, while the ZnO-MWCNT (5:1) composite displays a *p*-type sensing behavior. These observations indicate the major contribution of MWCNTs in determining the electrical conductivity and sensing performance of the composite. The DFT simulation results reveal that the SO_2 molecule interacts with the oxygen adatom of ZnO to form SO_3 and confirm the occurrence of charge transfer from ZnO to CNT which enhances the conductivity of the composite towards SO_2 gas. The present work is expected to promote future utilization of phytochemicals in the green synthesis of metal oxide-based nanocomposites and the theoretical simulation results will provide useful insights into the sensing mechanisms of metal oxide/CNT composites.

Acknowledgements

D.G. is grateful to the Australian Research Council (ARC) for granting a Laureate Fellowship (FL160100089) and to QUT project Nos. 323000-0355/51 and 323000-0348/07. The authors also acknowledge financial grants provided by Institut Teknologi Bandung (ITB, Indonesia), Ministry of Research, Technology, and Higher Education of Indonesia, Lembaga Pengelola Dana Pendidikan (LPDP), and Ministry of Finance of Indonesia. This work was performed in part at the Queensland node of the Australian National Fabrication Facility (ANFF), a company established under the National Collaborative Research Infrastructure Strategy to provide nano and microfabrication facilities for Australian researchers.

Associated Content

Supporting Information

The Supporting Information is available free of charge on the ACS Publications. Extraction of anthocyanin process; XRD patterns of MWCNTs before and after acid treatment; SEM images of ZnO products obtained with different amounts of anthocyanin; SEM images of the MWCNTs before and after acid treatment; TEM and HRTEM images of ZnO-MWCNT composites; UV-vis absorption spectra and Tauc's plots of ZnO and ZnO-MWCNT composites; N_2 sorption isotherms of functionalized MWCNTs; Arrhenius plots of ZnO and ZnO-MWCNT composites; Dynamic response-recovery curves of MWCNTs towards different concentrations of SO_2 gas at 300 °C; Comparison of the SO_2 sensing performance of the as-prepared ZnO-MWCNT (15:1) composite against previously reported metal oxide-based sensors.

Notes

The authors declare no competing financial interest.

Corresponding Authors

Email: KANETI.Valentino@nims.go.jp

Email brian@tf.itb.ac.id

Email: dmitry.golberg@qut.edu.au

Email: y.yamauchi@uq.edu.au

ORCID

Yusuf Valentino Kaneti: 0000-0003-2433-7305

Brian Yuliarto: 0000-0003-0662-7923

Hermawan Kresno Dipojono: 0000-0002-1391-3533

Dmitri Golberg: 0000-0003-2298-6539

Yusuke Yamauchi: 0000-0001-7854-927X

References

1. Septiani, N. L. W.; Kaneti, Y. V.; Yuliarto, B.; Nugraha; Dipojono, H. K.; Takei, T.; You, J.; Yamauchi, Y., Hybrid Nanoarchitecturing of Hierarchical Zinc Oxide Wool-Ball-like Nanostructures with Multi-Walled Carbon Nanotubes for Achieving Sensitive and Selective Detection of Sulfur Dioxide. *Sens. Actuators B* **2018,** *261*, 241-251.
2. Tyagi, P.; Sharma, S.; Tomar, M.; Singh, F.; Gupta, V., Swift Heavy Ion Irradiated SnO_2 Thin Film Sensor for Efficient Detection of SO_2 Gas. *Nucl. Instrum. Methods Phys. Res. B* **2016,** *379*, 219-223.
3. Wu, C.-M.; Baltrusaitis, J.; Gillan, E. G.; Grassian, V. H., Sulfur Dioxide Adsorption on ZnO Nanoparticles and Nanorods. *J. Phys. Chem. C* **2011,** *115*, 10164-10172.
4. Rodriguez, J. A.; Jirsak, T.; Chaturvedi, S.; Dvorak, J., Chemistry of SO_2 and NO_2 on ZnO(0001)-Zn and ZnO Powders: Changes in Reactivity with Surface Structure and Composition. *J. Mol. Catal. A* **2001,** *167*, 47-57.
5. Tyagi, P.; Sharma, A.; Tomar, M.; Gupta, V., Metal Oxide Catalyst Assisted SnO_2 Thin Film Based SO_2 Gas Sensor. *Sens. Actuators B* **2016,** *224*, 282-289.
6. Tyagi, P.; Sharma, A.; Tomar, M.; Gupta, V., A Comparative Study of RGO-SnO_2 and MWCNT-SnO_2 Nanocomposites Based SO_2 Gas Sensors. *Sens. Actuators B* **2017,** *248*, 980-986.
7. Tyagi, P.; Sharma, A.; Tomar, M.; Gupta, V., SnO_2 Thin Film Sensor Having NiO Catalyst for Detection of SO_2 Gas with Improved Response Characteristics. *Sens. Actuators B* **2017,** *248*, 998-1005.
8. Carrascon, V.; Ontañón, I.; Bueno, M.; Ferreira, V., Gas Chromatography-Mass Spectrometry Strategies for the Accurate and Sensitive Speciation of Sulfur Dioxide in Wine. *J. Chromatogr. A* **2017,** *1504*, 27-34.
9. Langenberg, S.; Schurath, U., Gas Chromatography using Ice-Coated Fused Silica Columns: Study of Adsorption of Sulfur Dioxide on Water Ice. *Atmos. Chem. Phys.* **2018,** *18*, 7527-7537.
10. Ben Youssef, I.; Alem, H.; Sarry, F.; Elmazria, O.; Jimenez Rioboo, R.; Arnal-Hérault, C.; Jonquières, A., Functional Poly(urethane-imide)s Containing Lewis Bases for SO_2 Detection by Love Surface Acoustic Wave Gas Micro-Sensors. *Sens. Actuators B* **2013,** *185*, 309-320.
11. Weng, W.; Aldén, M.; Li, Z., Quantitative SO_2 Detection in Combustion Environments Using Broad Band Ultraviolet Absorption and Laser-Induced Fluorescence. *Anal. Chem.* **2019,** *91*, 10849-10855.
12. Jung, G.; Jeong, Y.; Hong, Y.; Wu, M.; Hong, S.; Shin, W.; Park, J.; Jang, D.; Lee, J.-H., SO_2 Gas Sensing Characteristics of FET- and Resistor-Type Gas Sensors Having WO_3 as Sensing Material. *Solid State Electron.* **2020,** *165*, 107747.
13. Fitriana; Septiani, N. L. W.; Adhika, D. R.; Saputro, A. G.; Nugraha; Yuliarto, B., Enhanced NO Gas Performance of (002)-Oriented Zinc Oxide Nanostructure Thin Films. *IEEE Access* **2019,** *7*, 155446-155454.
14. Song, L.; Lukianov, A.; Butenko, D.; Li, H.; Zhang, J.; Feng, M.; Liu, L.; Chen, D.; Klyui, N. I., Facile Synthesis of Hierarchical Tin Oxide Nanoflowers with Ultra-High Methanol Gas Sensing at Low Working Temperature. *Nanoscale Res. Lett.* **2019,** *14*, 84.

15. Yu, H.-L.; Wang, J.; Zheng, B.; Zhang, B.-W.; Liu, L.-Q.; Zhou, Y.-W.; Zhang, C.; Xue, X.-L., Fabrication of Single Crystalline WO_3 Nano-Belts Based Photoelectric Gas Sensor for Detection of High Concentration Ethanol Gas at Room Temperature. *Sens. Actuators A* **2020,** *303*, 111865.

16. Patil, V. L.; Vanalakar, S. A.; Shendage, S. S.; Patil, S. P.; Kamble, A. S.; Tarwal, N. L.; Sharma, K. K.; Kim, J. H.; Patil, P. S., Fabrication of Nanogranular TiO_2 Thin Films by SILAR Technique: Application for NO_2 Gas Sensor. *Inorg. Nano-Metal Chem.* **2019,** *49*, 191-197.

17. Nakate, U. T.; Ahmad, R.; Patil, P.; Yu, Y. T.; Hahn, Y.-B., Ultra Thin NiO Nanosheets for High Performance Hydrogen Gas Sensor Device. *Appl. Surf. Sci.* **2020,** *506*, 144971.

18. Su, C.; Zhang, L.; Han, Y.; Chen, X.; Wang, S.; Zeng, M.; Hu, N.; Su, Y.; Zhou, Z.; Wei, H.; Yang, Z., Glucose-Assisted Synthesis of Hierarchical Flower-Like Co_3O_4 Nanostructures Assembled by Porous Nanosheets for Enhanced Acetone Sensing. *Sens. Actuators B* **2019,** *288*, 699-706.

19. Kaneti, Y. V.; Yue, J.; Moriceau, J.; Chen, C.; Liu, M.; Yuan, Y.; Jiang, X.; Yu, A., Experimental and Theoretical Studies on Noble Metal Decorated Tin Oxide Flower-Like Nanorods with High Ethanol Sensing Performance. *Sens. Actuators B* **2015,** *219*, 83-93.

20. Yang, X.; Salles, V.; Kaneti, Y. V.; Liu, M.; Maillard, M.; Journet, C.; Jiang, X.; Brioude, A., Fabrication of Highly Sensitive Gas Sensor Based on Au Functionalized WO_3 Composite Nanofibers by Electrospinning. *Sens. Actuators B* **2015,** *220*, 1112-1119.

21. Morisot, F.; Zuliani, C.; Luque, J.; Ali, Z.; Mouis, M.; Nguyen, V. H.; Muñoz-Rojas, D.; Lourhzal, O.; Texier, M.; Cornelius, T. W.; Ternon, C., ZnO Based Nanowire Network for Gas Sensing Applications. *Mater. Res. Exp.* **2019,** *6*, 084004.

22. Chao, J.; Chen, Y.; Xing, S.; Zhang, D.; Shen, W., Facile Fabrication of ZnO/C Nanoporous Fibers and ZnO Hollow Spheres for High Performance Gas Sensor. *Sens. Actuators B* **2019,** *298*, 126927.

23. Bhati, V. S.; Hojamberdiev, M.; Kumar, M., Enhanced Sensing Performance of ZnO Nanostructures-Based Gas Sensors: A Review. *Energy Rep.* **2020,** *6*, 46-62.

24. Kaneti, Y. V.; Zhang, X.; Liu, M.; Yu, D.; Yuan, Y.; Aldous, L.; Jiang, X., Experimental and Theoretical Studies of Gold Nanoparticle Decorated Zinc Oxide Nanoflakes with Exposed $\{101\bar{0}\}$ Facets for Butylamine Sensing. *Sens. Actuators B* **2016,** *230*, 581-591.

25. Xu, J.; Xue, Z.; Qin, N.; Cheng, Z.; Xiang, Q., The Crystal Facet-Dependent Gas Sensing Properties of ZnO Nanosheets: Experimental and Computational Study. *Sens. Actuators B* **2017,** *242*, 148-157.

26. Mani, G. K.; Rayappan, J. B. B., Facile Synthesis of ZnO Nanostructures by Spray Pyrolysis Technique and Its Application as Highly Selective H_2S Sensor. *Mater. Lett.* **2015,** *158*, 373-376.

27. Kaneti, Y. V.; Yue, J.; Jiang, X.; Yu, A., Controllable Synthesis of ZnO Nanoflakes with Exposed $(10\bar{1}0)$ for Enhanced Gas Sensing Performance. *J. Phys. Chem. C* **2013,** *117*, 13153-13162.

28. Yuliarto, B.; Ramadhani, M. F.; Nugraha; Septiani, N. L. W.; Hamam, K. A., Enhancement of SO_2 Gas Sensing Performance using ZnO Nanorod Thin Films: The Role of Deposition Time. *J. Mater. Sci.* **2017,** *52*, 4543-4554.

29. Navale, Y. H.; Navale, S. T.; Stadler, F. J.; Ramgir, N. S.; Patil, V. B., Enhanced NO_2 Sensing Aptness of ZnO Nanowire/CuO Nanoparticle Heterostructure-Based Gas Sensors. *Ceram. Int.* **2019,** *45*, 1513-1522.

30. Jamshidi Bandari, A.; Nasirian, S., Carbon Monoxide Gas Sensing Features of Zinc Oxide Nanoneedles: Practical Selectivity and Long-Term Stability. *J. Mater. Sci.* **2019,** *30*, 10073-10081.

31. Wang, J.; Yu, M.; Xia, Y.; Li, X.; Yang, C.; Komarneni, S., On-Chip Grown ZnO Nanosheet-Array with Interconnected Nanojunction Interfaces for Enhanced Optoelectronic NO_2 Gas Sensing at Room Temperature. *J. Colloid Interface Sci.* **2019,** *554*, 19-28.

32. Kanaparthi, S.; Govind Singh, S., Highly Sensitive and Ultra-Fast Responsive Ammonia Gas Sensor Based on 2D ZnO Nanoflakes. *Mater. Sci. Energy Technol.* **2020,** *3*, 91-96.

33. Feng, Z.; Gao, C.; Ma, X.; Zhan, J., Well-Dispersed Pd Nanoparticles on Porous ZnO Nanoplates via Surface Ion Exchange for Chlorobenzene-Selective Sensor. *RSC Adv.* **2019,** *9*, 42351-42359.

34. Tao, Z.; Li, Y.; Sun, G.; Xiao, M., Enhanced TEA Sensing Properties of Nest-Like ZnO by Decoration with Au. *Mater. Res. Exp.* **2019,** *6*, 105910.

35. Patra, A. K.; Dutta, A.; Bhaumik, A., Self-Assembled Ultra Small ZnO Nanocrystals for Dye-Sensitized Solar Cell Application. *J. Solid State Chem.* **2014,** *215*, 135-142.

36. Chandra, D.; Mridha, S.; Basak, D.; Bhaumik, A., Template Directed Synthesis of Mesoporous ZnO Having High Porosity and Enhanced Optoelectronic Properties. *Chem. Commun.* **2009,** *17*, 2384-2386.

37. Lin, Z.; Guo, F.; Wang, C.; Wang, X.; Wang, K.; Qu, Y., Preparation and Sensing Properties of Hierarchical 3D Assembled Porous ZnO from Zinc Hydroxide Carbonate. *RSC Adv.* **2014,** *4*, 5122-5129.

38. Gröttrup, J.; Paulowicz, I.; Schuchardt, A.; Kaidas, V.; Kaps, S.; Lupan, O.; Adelung, R.; Mishra, Y. K., Three-Dimensional Flexible Ceramics Based on Interconnected Network of Highly Porous Pure and Metal Aloyed ZnO Tetrapods. *Ceram. Int.* **2016,** *42*, 8664-8676.

39. Kaneti, Y. V.; Wulan Septiani, N. L.; Saptiama, I.; Jiang, X.; Yuliarto, B.; Shiddiky, M. J. A.; Fukumitsu, N.; Kang, Y.-M.; Golberg, D.; Yamauchi, Y., Self-Sacrificial Templated Synthesis of a Three-Dimensional Hierarchical Macroporous Honeycomb-Like ZnO/$ZnCo_2O_4$ Hybrid for Carbon Monoxide Sensing. *J. Mater. Chem. A* **2019,** *7*, 3415-3425.

40. Nagajyothi, P. C.; Lim, H.; Shim, J.; Rawal, S. B., Au Nanoparticles Supported Nanoporous ZnO Sphere for Enhanced Photocatalytic Activity Under UV-Light Irradiation. *J. Cluster Sci.* **2016,** *27*, 1159-1170.

41. Yang, C.; Li, Q.; Tang, L.; Bai, A.; Song, H.; Yu, Y., Monodispersed Colloidal Zinc Oxide Nanospheres with Various Size Scales: Synthesis, Formation Mechanism, and Enhanced Photocatalytic Activity. *J. Mater. Sci.* **2016,** *51*, 5445-5459.

42. Tripathy, N.; Ahmad, R.; Kuk, H.; Lee, D. H.; Hahn, Y. B.; Khang, G., Rapid Methyl Orange Degradation using Porous ZnO Spheres Photocatalyst. *J Photochem. Photobiol. B* **2016,** *161*, 312-7.

43. Singh, S.; Srivastava, V. C.; Lo, S. L.; Mandal, T. K.; Naresh, G., Morphology-Controlled Green Approach for Synthesizing the Hierarchical Self-Assembled 3D Porous ZnO Superstructure with Excellent Catalytic Activity. *Microporous Mesoporous Mater.* **2017,** *239*, 296-309.

44. Agarwal, H.; Venkat Kumar, S.; Rajeshkumar, S., A Review on Green Synthesis of Zinc Oxide Nanoparticles – An Eco-Friendly Approach. *Res.-Eff. Technol.* **2017,** *3*, 406-413.

45. Yuliarto, B.; Septiani, N. L. W.; Kaneti, Y. V.; Iqbal, M.; Gumilar, G.; Kim, M.; Na, J.; Wu, K. C. W.; Yamauchi, Y., Green Synthesis of Metal Oxide Nanostructures using Naturally Occurring Compounds for Energy, Environmental, and Bio-Related Applications. *New J. Chem.* **2019,** *43*, 15846-15856.

46. Diallo, A.; Ngom, B. D.; Park, E.; Maaza, M., Green Synthesis of ZnO Nanoparticles by Aspalathus Linearis: Structural & Optical Properties. *J. Alloys Compd.* **2015,** *646*, 425-430.

47. Sundrarajan, M.; Ambika, S.; Bharathi, K., Plant-Extract Mediated Synthesis of ZnO Nanoparticles using Pongamia Pinnata and Their Activity Against Pathogenic Bacteria. *Adv. Powder Tech.* **2015,** *26*, 1294-1299.

48. Sangeetha, G.; Rajeshwari, S.; Venckatesh, R., Green Synthesis of Zinc Oxide Nanoparticles by Aloe Barbadensis Miller Leaf Extract: Structure and Optical Properties. *Mater. Res. Bull.* **2011,** *46*, 2560-2566.

49. Karnan, T.; Selvakumar, S. A. S., Biosynthesis of ZnO Nanoparticles using Rambutan (Nephelium Lappaceum L.) Peel Extract and Their Photocatalytic Activity on Methyl Orange Dye. *J. Mol. Struct.* **2016,** *1125*, 358-365.

50. Yuvakkumar, R.; Suresh, J.; Nathanael, A. J.; Sundrarajan, M.; Hong, S. I., Novel Green Synthetic Strategy to Prepare ZnO Nanocrystals using Rambutan (Nephelium lappaceum L.) Peel Extract and Its Antibacterial Applications. *Mat. Sci. Eng. C* **2014,** *41*, 17-27.

51. Singh, G.; Choudhary, A.; Haranath, D.; Joshi, A. G.; Singh, N.; Singh, S.; Pasricha, R., ZnO Decorated Luminescent Graphene as a Potential Gas Sensor at Room Temperature. *Carbon* **2012,** *50*, 385-394.

52. Ha, N. H.; Thinh, D. D.; Huong, N. T.; Phuong, N. H.; Thach, P. D.; Hong, H. S., Fast Response of Carbon Monoxide Gas Sensors using a Highly Porous Network of ZnO Nanoparticles Decorated on 3D Reduced Graphene Oxide. *Appl. Surf. Sci.* **2018,** *434*, 1048-1054.

53. Utari, L.; Septiani, N. L. W.; Suyatman; Nugraha; Nur, L. O.; Wasisto, H. S.; Yuliarto, B., Wearable Carbon Monoxide Sensors Based on Hybrid Graphene/ZnO Nanocomposites. *IEEE Access* **2020,** *8*, 49169-49179.

54. Huang, G.; Zhang, F.; Du, X.; Qin, Y.; Yin, D.; Wang, L., Metal Organic Frameworks Route to in Situ Insertion of Multiwalled Carbon Nanotubes in Co_3O_4 Polyhedra as Anode Materials for Lithium-Ion Batteries. *ACS Nano* **2015,** *9*, 1592-1599.

55. Cui, H.; Yan, C.; Jia, P.; Cao, W., Adsorption and Sensing Behaviors of SF_6 Decomposed Species on Ni-Doped C_3N Monolayer: A First-Principles Study. *Appl. Surf. Sci.* **2020,** *512*, 145759.

56. Cui, H.; Jia, P.; Peng, X., Adsorption of SO_2 and NO_2 Molecule on Intrinsic and Pd-Doped $HfSe_2$ Monolayer: A First-Principles Study. *Appl. Surf. Sci.* **2020,** *513*, 145863.

57. Zhang, X.; Yu, L.; Wu, X.; Hu, W., Experimental Sensing and Density Functional Theory Study of H_2S and SOF_2 Adsorption on Au-Modified Graphene. *Adv. Sci.* **2015,** *2*, 1500101.

58. Zhang, X.; Dai, Z.; Wei, L.; Liang, N.; Wu, X., Theoretical Calculation of the Gas-Sensing Properties of Pt-Decorated Carbon Nanotubes. *Sensors* **2013,** *13*, 15159-15171.

59. Saputro, A. G.; Akbar, F. T.; Setyagar, N. P. P.; Agusta, M. K.; Pramudya, A. D.; Dipojono, H. K., Effect of Surface Defects on the Interaction of the Oxygen Molecule with the ZnO(10$\bar{1}$0) Surface. *New J. Chem.* **2020,** *44*, 7376-7385.

60. Nugraha; Saputro, A. G.; Agusta, M. K.; Yuliarto, B.; Dipojono, H. K.; Rusydi, F.; Maezono, R., Selectivity of CO and NO Adsorption on ZnO (0002) Surfaces: A DFT Investigation. *Appl. Surf. Sci.* **2017,** *410*, 373-382.

61. Nugraha; Saputro, A. G.; Agusta, M. K.; Yuliarto, B.; Dipojono, H. K.; Maezono, R., Density functional Study of Adsorptions of CO_2, NO_2 and SO_2 Molecules on Zn(0002) Surfaces. *J. Phys. Chem. C* **2016,** *739*, 012080.

62. Nugraha; Saputro, A. G.; Agusta, M. K.; Akbar, F. T.; Pramudya, A. D., Density Functional Study on Benzene, Toluene, Ethylbenzene and Xylene Adsorptions on ZnO(100) Surface. *Molekul* **2019,** *14*, 37-47.

63. Chai, G.-L.; Lin, C.-S.; Cheng, W.-D., First-Principles Study of ZnO Cluster-Decorated Carbon Nanotubes. *Nanotechnology* **2011,** *22*, 445705.

64. Zhang, S.; Zhang, Y.; Huang, S.; Liu, H.; Wang, P.; Tian, H., First-Principles Study of Field Emission Properties of Graphene-ZnO Nanocomposite. *J. Phys. Chem. C* **2010,** *114*, 19284-19288.

65. Sezer, N.; Koç, M., Oxidative Acid Treatment of Carbon Nanotubes. *Surf. Interfaces* **2019,** *14*, 1-8.

66. Giannozzi, P.; Baroni, S.; Bonini, N.; Calandra, M.; Car, R.; Cavazzoni, C.; Ceresoli, D.; Chiarotti, G. L.; Cococcioni, M.; Dabo, I.; Dal Corso, A.; de Gironcoli, S.; Fabris, S.; Fratesi, G.; Gebauer, R.; Gerstmann, U.; Gougoussis, C.; Kokalj, A.; Lazzeri, M.; Martin-Samos, L.; Marzari, N.; Mauri, F.; Mazzarello, R.; Paolini, S.; Pasquarello, A.; Paulatto, L.; Sbraccia, C.; Scandolo, S.; Sclauzero, G.; Seitsonen, A. P.; Smogunov, A.; Umari, P.; Wentzcovitch, R. M., QUANTUM ESPRESSO: A Modular and Open-Source Software Project for Quantum Simulations of Materials. *J. Phys. Cond. Matter* **2009,** *21*, 395502.

67. Perdew, J. P.; Burke, K.; Ernzerhof, M., Generalized Gradient Approximation Made Simple. *Phys. Rev. Lett.* **1996,** *77*, 3865-3868.

68. Blöchl, P. E., Projector Augmented-Wave Method. *Phys. Rev. B* **1994,** *50*, 17953-17979.

69. Sanville, E.; BelBruno, J. J., Electronic and Geometric Structure Calculations of Adsorption of Small $(ZnO)_i$ Clusters (i = 1-4) on Graphite. *Phys. Rev. B* **2007,** *76*, 085412.

70. Kokalj, A., Computer Graphics and Graphical User Interfaces as Tools in Simulations of Matter at the Atomic Scale. *Comp. Mater. Sci.* **2003,** *28*, 155-168.

71. Prima, E. C.; Al Qibtiya, M.; Yuliarto, B.; Suyatman; Dipojono, H. K., Influence of Anthocyanin Co-Pigment on Electron Transport and Performance in Black Rice Dye-Sensitized Solar Cell. *Ionics* **2016,** *22*, 1687-1697.

72. Lee, J. H., Identification and Quantification of Anthocyanins from the Grains of Black Rice (Oryza sativa L.) Varieties. *Food Sci. Biotechnol.* **2010,** *19*, 391-397.

73. Pedro, A. C.; Granato, D.; Rosso, N. D., Extraction of Anthocyanins and Polyphenols from Black Rice (Oryza sativa L.) by Modeling and Assessing Their Reversibility and Stability. *Food Chem.* **2016,** *191*, 12-20.

74. Frank, T.; Reichardt, B.; Shu, Q.; Engel, K.-H., Metabolite Profiling of Colored Rice (Oryza sativa L.) Grains. *J. Cereal Sci.* **2012,** *55*, 112-119.

75. Escribano-Bailón, M. T.; Santos-Buelga, C.; Rivas-Gonzalo, J. C., Anthocyanins in Cereals. *J. Chromatogr. A* **2004,** *1054*, 129-141.

76. Kaneti, Y. V.; Zhang, Z.; Yue, J.; Zakaria, Q. M. D.; Chen, C.; Jiang, X.; Yu, A., Crystal Plane-Dependent Gas-Sensing Properties of Zinc Oxide Nanostructures: Experimental and Theoretical Studies. *Phys. Chem. Chem. Phys.* **2014,** *16*, 11471-11480.

77. Tian, S.; Yang, F.; Zeng, D.; Xie, C., Solution-Processed Gas Sensors Based on ZnO Nanorods Array with an Exposed (0001) Facet for Enhanced Gas-Sensing Properties. *J. Phys. Chem. C* **2012,** *116*, 10586-10591.

78. Nayak, B.; Berrios, J. D. J.; Powers, J. R.; Tang, J., Thermal Degradation of Anthocyanins from Purple Potato (Cv. Purple Majesty) and Impact on Antioxidant Capacity. *J. Agric. Food Chem.* **2011,** *59*, 11040-11049.

79. Zhang, W.-D.; Xu, B.; Jiang, L.-C., Functional Hybrid Materials Based on Carbon Nanotubes and Metal Oxides. *J. Mater. Chem.* **2010,** *20*, 6383-6391.

80. Bhat, P.; K, N. K. S.; Nagaraju, P., Synthesis and Characterization of ZnO-MWCNT Nanocomposites for 1-Butanol Sensing Application at Room Temperature. *Phys. B. Condens. Matter* **2019,** *570*, 139-147.

81. Supraja, P.; Singh, V.; Vanjari, S. R. K.; Govind Singh, S., Electrospun CNT Embedded ZnO Nanofiber Based Biosensor for Electrochemical Detection of Atrazine: A Step Closure to Single Molecule Detection. *Microsyst. Nanoeng.* **2020,** *6*, 3.

82. Kaneti, Y. V.; Liu, M.; Zhang, X.; Bu, Y.; Yuan, Y.; Jiang, X.; Yu, A., Synthesis of Platinum-Decorated Iron Vanadate Nanorods with Excellent Sensing Performance toward n-Butylamine. *Sens. Actuators B* **2016,** *236*, 173-183.

83. Septiani, N. L. W.; Yuliarto, B.; Nugraha; Dipojono, H. K., Multiwalled Carbon Nanotubes–Zinc Oxide Nanocomposites as Low Temperature Toluene Gas Sensor. *Appl. Phys. A* **2017,** *123*, 166.

84. Naghadeh, S. B.; Vahdatifar, S.; Mortazavi, Y.; Khodadadi, A. A.; Abbasi, A., Functionalized MWCNTs Effects on Dramatic Enhancement of MWCNTs/SnO_2 Nanocomposite Gas Sensing Properties at Low Temperatures. *Sens. Actuators B* **2016,** *223*, 252-260.

85. Dai, M.; Zhao, L.; Gao, H.; Sun, P.; Liu, F.; Zhang, S.; Shimanoe, K.; Yamazoe, N.; Lu, G., Hierarchical Assembly of α-Fe_2O_3 Nanorods on Multiwall Carbon Nanotubes as a High-Performance Sensing Material for Gas Sensors. *ACS Appl. Mater. Interfaces* **2017,** *9*, 8919-8928.

86. Liu, C.; Zhao, L.; Wang, B.; Sun, P.; Wang, Q.; Gao, Y.; Liang, X.; Zhang, T.; Lu, G., Acetone Gas Sensor Based on NiO/ZnO Hollow Spheres: Fast Response and Recovery, and Low (ppb) Detection Limit. *J. Colloid Interface Sci.* **2017,** *495*, 207-215.

87. Van Tong, P.; Hoa, N. D.; Nha, H. T.; Van Duy, N.; Hung, C. M.; Van Hieu, N., SO_2 and H_2S Sensing Properties of Hydrothermally Synthesized CuO Nanoplates. *J. Electron. Mater.* **2018,** *47*, 7170-7178.

88. Zhou, Q.; Xie, B.; Jin, L.; Chen, W.; Li, J., Hydrothermal Synthesis and Responsive Characteristics of Hierarchical Zinc Oxide Nanoflowers to Sulfur Dioxide. *J. Nanotechnol.* **2016,** *2016*, 6742104.

89. Ma, X.; Qin, Q.; Zhang, N.; Chen, C.; Liu, X.; Chen, Y.; Li, C.; Ruan, S., Synthesis of SnO_2 Nano-Dodecahedrons with High-Energy Facets and Their Sensing Properties to SO_2 at Low Temperature. *J. Alloys Compd.* **2017,** *723*, 595-601.

90. Boudiba, A.; Zhang, C.; Bittencourt, C.; Umek, P.; Olivier, M.-G.; Snyders, R.; Debliquy, M., SO_2 Gas Sensors based on WO_3 Nanostructures with Different Morphologies. *Proc. Eng.* **2012,** *47*, 1033-1036.

91. Das, S.; Rana, S.; Mursalin, S. M.; Rana, P.; Sen, A., Sonochemically Prepared Nanosized $BiFeO_3$ as Novel SO_2 Sensor. *Sens. Actuator B* **2015,** *218*, 122-127.

92. Liu, H.; Zhou, Q.; Zhang, Q.; Hong, C.; Xu, L.; Jin, L.; Chen, W., Synthesis, Characterization and Enhanced Sensing Properties of a NiO/ZnO p–n Junctions Sensor for the SF_6 Decomposition Byproducts SO_2, SO_2F_2, and SOF_2. *Sensors* **2017,** *17*, 913.

93. Zhou, Q.; Zeng, W.; Chen, W.; Xu, L.; Kumar, R.; Umar, A., High Sensitive and Low-Concentration Sulfur Dioxide (SO_2) Gas Sensor Application of Heterostructure NiO-ZnO Nanodisks. *Sens. Actuator B* **2019,** *298*, 126870.

94. El Morabet, R., Effects of Outdoor Air Pollution on Human Health. In *Encyclopedia of Environmental Health (Second Edition)*, Nriagu, J., Ed. Elsevier: Oxford, 2019; pp 278-286.

95. Doble, M.; Kumar, A., CHAPTER 30 - Gaseous Pollutants and Volatile Organics. In *Biotreatment of Industrial Effluents*, Butterworth-Heinemann: Burlington, 2005; pp 301-312.

96. Nugraha; Saputro, A. G.; Agusta, M. K.; Yuliarto, B.; Dipojono, H. K.; Maezono, R., Density Functional Study of Adsorptions of CO_2, NO_2 and SO_2 Molecules on Zn(0002) Surfaces. *J. Phys. Conf. Ser.* **2016,** *739*, 012080.

97. Babu, D. J.; Puthusseri, D.; Kühl, F. G.; Okeil, S.; Bruns, M.; Hampe, M.; Schneider, J. J., SO_2 Gas Adsorption on Carbon Nanomaterials: A Comparative Study. *Beilstein J. Nanotechnol.* **2018,** *9*, 1782-1792.

98. Hunter, G. W.; Akbar, S.; Bhansali, S.; Daniele, M.; Erb, P. D.; Johnson, K.; Liu, C.-C.; Miller, D.; Oralkan, O.; Hesketh, P. J.; Manickam, P.; Vander Wal, R. L., A Critical Review of Solid State Gas Sensors. *J. Electrochem. Soc.* **2020,** *167*, 037570.

99. Darvishnejad, M. H.; Anaraki Firooz, A.; Beheshtian, J.; Khodadadi, A. A., Highly Sensitive and Selective Ethanol and Acetone Gas Sensors by Adding Some Dopants (Mn, Fe, Co, Ni) onto Hexagonal ZnO Plates. *RSC Adv.* **2016,** *6*, 7838-7845.

100. Al-Hadeethi, Y.; Umar, A.; Ibrahim, A. A.; Al-Heniti, S. H.; Kumar, R.; Baskoutas, S.; Raffah, B. M., Synthesis, Characterization and Acetone Gas Sensing Applications of Ag-Doped ZnO Nanoneedles. *Ceram. Int.* **2017,** *43*, 6765-6770.

101. Hojati, T.; Ebrahimi, M.; Afzalzadeh, R., Highly Sensitive CO Sensor Based on ZnO/MWCNT Nano Sheet Network Grown via Hydrothermal Method. *Mater. Chem. Phys.* **2018,** *207*, 50-57.

102. Li, Z.; Li, H.; Wu, Z.; Wang, M.; Luo, J.; Torun, H.; Hu, P.; Yang, C.; Grundmann, M.; Liu, X.; Fu, Y., Advances in Designs and Mechanisms of Semiconducting Metal Oxide Nanostructures for High-Precision Gas Sensors Operated at Room Temperature. *Mater. Horiz.* **2019,** *6*, 470-506.

103. Jayababu, N.; Poloju, M.; Shruthi, J.; Reddy, M. V. R., NiO Decorated CeO_2 Nanostructures as Room Temperature Isopropanol Gas Sensors. *RSC Adv.* **2019,** *9*, 13765-13775.

104. Chen, M.; Straatsma, T. P.; Fang, Z.; Dixon, D. A., Structural and Electronic Property Study of $(ZnO)_n$, $n \leq 168$: Transition from Zinc Oxide Molecular Clusters to Ultrasmall Nanoparticles. *J. Phys. Chem. C* **2016,** *120*, 20400-20418.

TABLE OF CONTENT (TOC) GRAPHIC DESCRIPTION

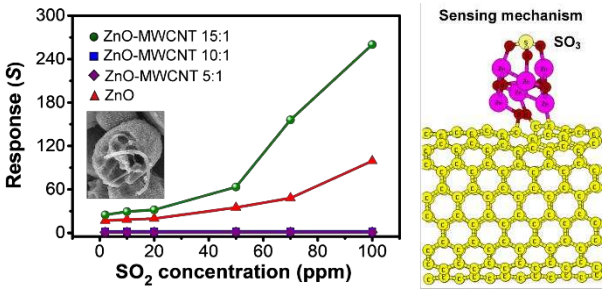

This work reports the green synthesis of ZnO-MWCNT composite using anthocyanin extracted from black rice grains with high sensitivity and selectivity to SO_2 and its sensing mechanism study by DFT simulations.